Title

Smc5/6 - microtubules binding shapes pericentromeric chromatin

Author list

Ànnia Carré-Simon[1,6]*, Cecilia Martuzzi[1#], Sarah Isler[2#], Renaud Batrin[1], Henrik Dahl Pinholt[3], Timothy Földes[4], Guillaume Laflamme[2], Maria Barbi[4], Leonid Mirny[3,5], Damien D'Amours[2], Emmanuelle Fabre[1]*

Authors affiliations

[1]Université de Paris Cité, INSERM, CNRS, IRSL, U1342, EMR8000, Paris, France

[2]Ottawa Institute of Systems Biology, Department of Cellular and Molecular Medicine, Ottawa, Canada

[3]Department of Physics, Massachusetts Institute of Technology, Cambridge, MA, USA.

[4] Sorbonne Université, CNRS, LPTMC, Paris, France

[5]Institute for Medical Engineering and Science, Massachusetts Institute of Technology, Cambridge, MA, USA

[6] Present address: Department of Pathology, NYU Grossman School of Medicine, New York, NY, USA.

# equal contribution

*Correspondance : emmanuelle-g.fabre@inserm.fr

*Correspondance : annia.carresimon@nyulangone.org

Abstract

Centromeres and pericentromeres are specialized chromatin regions essential for accurate chromosome segregation. Smc5/6, which localizes at pericentromeres, can bind microtubules, yet its role in chromatin folding is unclear. Here, we investigate the functional relevance of Smc5/6- microtubule binding in yeast, by targeting two lysines (K624, K631) within the Smc5 hinge domain known to mediate this binding. Using high-temporal-resolution imaging, polymer modelling, and *in vitro* approaches with a separation-of-function mutant *smc5-2KE*, we demonstrate that microtubules binding by Smc5/6 constrains chromatin dynamics and promotes pericentromeric folding. The *smc5-2KE* mutant, combined with a hypomorphic kinetochore mutant (Mtw1-3xGFP), leads to spindle and cytokinesis defects and triggers the spindle checkpoint. Furthermore, homologous recombination repair in pericentromeres is compromised. Overall, our findings indicate that Smc5/6 – microtubules association safeguard pericentromeric architecture and genome stability during mitosis.

Key words

Smc5/6, microtubules, pericentromeres, mitotic spindle, DNA double-strand break repair, chromatin dynamics.

Introduction

The three-dimensional architecture of the genome governs gene expression, DNA replication and repair (Misteli, 2020). Centromeres are specialized regions within this chromosomal architecture that serve as scaffolds for microtubule attachment via the kinetochore, a complex of around 80 proteins (Biggins, 2013; Talbert and Henikoff, 2020). Surrounding the centromere, pericentromeric regions adopt a distinct chromatin configuration that is essential for genome stability (Bloom, 2024). Pericentromeric configuration and centromere/kinetochore assembly are crucial to counterbalance the mechanical forces exerted by spindle microtubules during mitosis. Yet, how pericentromeric structure is shaped to resist the forces exerted by microtubules is poorly understood (Harasymiw et al., 2019; Stephens et al., 2011). In budding yeast, pericentromeres span around 30-50 kb (Paldi et al., 2020) and are highly enriched in structural chromosome maintenance (SMC) complexes, which include cohesins, condensins and the Smc5/6 complex (Smc5/6 in short) (D'Ambrosio et al., 2008; Jeppsson et al., 2014; Megee et al., 1999; Tanaka et al., 1999). Cohesins and condensins participate in the establishment of DNA loops that resist mitotic spindle forces (Lawrimore and Bloom, 2022). While assembly of an Smc5/6 dimer was recently shown to contribute to DNA loop folding *in vitro* (Pradhan et al., 2023), the folding function of Smc5/6 at pericentromeres is unknown.

Smc5/6 is composed of Smc5, Smc6 and non-SMC proteins (Nse1, Mms21 and Nse3-6) (Roy et al., 2024). Smc5 and Smc6 consist of antiparallel coiled-coil arms that dimerize via a hinge domain at one end and are linked at the other end by their ATPase head domains. As a key player in genome stability that mediates post-translational modifications (PTMs), Smc5/6 interacts with many chromosome proteins during its cellular functions (Roy et al., 2024). One of the most intriguing interactors of the complex is the alpha/beta tubulin dimer. We previously showed *in vitro* that the hinge domain of the Smc5 protein binds the tubulin dimer exclusively in the form of microtubule polymers. The hinge domain contains three lysines (K624, K631 and K667) that interact directly *in vitro* with the C-terminal negatively charged tails of tubulins (Laflamme et al., 2014). A recent mass spectrometry analysis of overexpressed Smc5/6 purified from exponentially growing yeast, which we have confirmed, also identified alpha/beta tubulin subunits Tub1 and Tub2, as cofactors binding to the Smc5/6 complex

70 (Gutierrez-Escribano et al., 2020, Figure supplement 1A-C). These data support an interaction
71 between the Smc5/6 complex and microtubules, but the function of such a link remains an
72 open question.

73 Besides its enrichment at pericentromeres, Smc5/6 is also found at telomeres and rDNA to
74 maintain their organization (Moradi-Fard et al., 2016; Torres-Rosell et al., 2005; Zhao and
75 Blobel, 2005). For example, deletion of the Nse2/Mms21 subunit of the Smc5/6 leads to
76 defects in genome organization, including telomere declustering and nucleolar fragmentation
77 (Moradi-Fard et al., 2016; Torres-Rosell et al., 2005; Zhao and Blobel, 2005). Additionally,
78 smc5/6 mutants (*smc6-9*) exhibit chromosome segregation defects, notably in repetitive
79 regions such as rDNA and telomeres (Torres-Rosell et al., 2007, 2005). Beyond its structural
80 role, Smc5/6 participates in genome integrity by promoting the repair of damaged
81 DNA(Aragón, 2018; Roy et al., 2024). Smc5/6 is recruited within ~5kb of double strand breaks
82 (DSB (De Piccoli et al., 2006; Lindroos et al., 2006), holds the DSB ends together (Phipps et al.,
83 2024) and facilitates homologous recombination (HR) (Ampatzidou et al., 2006; Bermúdez-
84 López et al., 2010; Pebernard et al., 2006; Torres-Rosell et al., 2005), a DNA repair process
85 that uses a homologous sequence as a template to accurately repair DSBs (Symington and
86 Gautier, 2011).

87 Here, we examine the role that the association between Smc5/6 and microtubules plays in
88 pericentromeric chromatin folding. We combine mutational analysis and fluorescence
89 microscopy in living cells with polymer simulations to show that the association between
90 microtubules and Smc5/6 impacts pericentromeric chromatin folding, dynamics and integrity.

91 Results

92 The *smc5-2KE* mutant leads to increased chromatin dynamics at pericentromeres.

93 To determine how Smc5/6 and microtubules could interact, we analyzed the spatial
94 distribution of K624, K631 and K667 residues using USCF Chimera based on the hinge domain
95 (PDB:7YLM (Li et al., 2024)). Our structural assessment revealed that K624 and K631 are
96 positioned on the outer surface of the hinge domain, making them accessible for potential
97 interactions with microtubules. In contrast, K667 is embedded in the coiled-coil arm of Smc5

98 and could not theoretically interact with microtubules (**Figure 1A**). These results agree with
99 the position of K624 and K631 in the specific loop of the C domain unique to the Smc5/6
100 according to the X-ray crystal structures of the *S. pombe* Smc5 hinge domain (Alt et al., 2017).

101 In a second step, using AlphaFold3 to model alpha/beta tubulin subunits and a segment of
102 the Smc5 hinge domain containing lysines K624 and K631 we identified a high probability of
103 interaction between this region and microtubules (iPTM = 0.72) (**Figure 1B**), in contrast with
104 the low probability of interaction with other proteins such as actin (iPTM=0.16) or the subunit
105 Shs1 of the septin complex (iPTM=0.18) (**Figure supplement 2A**).

106 This observation led us to focus on K624 and K631 and modify their electrostatic attraction
107 with the C-terminal tubulin tails by mutating them to negatively charged glutamic acid
108 residues, generating the *smc5-2KE* mutant (Material and methods and Laflamme et al., 2014).
109 The microtubule-binding capacity of the *smc5-2KE* mutant was verified *in vitro* by comparing
110 the co-sedimentation of purified Smc5 and Smc5-2KE proteins with microtubules. We
111 observed a 3-fold reduction in the binding affinity of Smc5-2KE compared to wild-type (WT)
112 Smc5 (**Figure 1 C – Figure supplement 2B**). The reduced affinity of Smc5-2KE for microtubules
113 was not due to a defect in the mutant's interaction with other proteins in the Smc5/6
114 complex, as indicated by co-immunoprecipitation (CoIP) of the Nse3 subunit with both WT
115 Smc5 and the Smc5-2KE (**Figure 1D**). The preservation of Smc5/6 function in the *smc5-2KE*
116 mutant is consistent with the absence of significant defects in cell growth, cell division, cell
117 cycle progression, sensitivity to DNA damage agents or thermosensitivity, as demonstrated in
118 mutated cells (**Figure supplement 2C-H**). Furthermore, the *smc5-2KE* mutant did not impact
119 the binding with DNA, as observed by ChIP-qPCR at centromeres, telomeres and rDNA (**Figure**
120 **supplement 2I**), indicating that the associations of Smc5/6 with microtubules and with
121 chromatin are independent. Therefore, we used *smc5-2KE* as a separation-of-function mutant
122 that is specifically defective in microtubule binding, to explore the role of Smc5/6 association
123 to microtubules in chromatin folding and dynamics *in vivo*.

124 To first investigate the impact of weakened microtubule-Smc5/6 association on chromatin
125 dynamics as a function of chromosome position, we tracked a GFP-labelled chromatin array
126 (tetO-TetR-GFP) positioned at 11, 90, and 730 kb from centromere IV (CEN IV) in both WT and
127 *smc5-2KE* mutant. We calculated the mean square displacement (MSD) as previously

128 described and extracted different dynamic parameters (Cabal et al., 2006; García Fernández
129 et al., 2021; Hajjoul et al., 2013; Herbert et al., 2017; Marshall et al., 1997; Miné-Hattab et al.,
130 2017; Miné-Hattab and Rothstein, 2012) (Material and methods). In WT cells, the different
131 tracked loci followed a sub-diffusive movement characterized by an anomalous α exponent
132 below 1.0 (between 0.59 and 0.61, **Figure 1E - Figure supplement 3A**). These values of α,
133 typical of self-avoiding bead-spring polymer models (Panja and Barkema, 2009), indicate that
134 the connectivity of the chromosome, qualitatively determining the nature of its dynamics, is
135 independent of its distance from the centromere. However, the sub-diffusive coefficient D,
136 as well as MSD at 10s (MSD_{10s}), indicated higher mobility at positions further from the
137 centromeric attachment point to kinetochore microtubules on CEN IV, as previously
138 documented (**Figure 1E,F - Figure supplement 3A-C**) (Cabal et al., 2006; Hajjoul et al., 2013;
139 Herbert et al., 2017; Neumann et al., 2012; Verdaasdonk et al., 2013). Interestingly, sub-
140 diffusive chromatin motion was maintained in *smc5-2KE* mutated cells with a similar α
141 parameter, but chromatin dynamics increased, characterized by an increase in D, at all loci
142 compared to WT cells. An increase in D can be explained by a decrease of interactions within
143 the chromatin polymer or with external factors, consistent with the loss of centromeric
144 constraint and/or partial detachment of centromeric chromatin from kinetochore
145 microtubules (Socol et al., 2019). Of note, the increase in chromatin dynamics in mutated cells
146 was more pronounced the closer the locus was to the centromere (**Figure 1E,F**). MSD_{10s}
147 increased in the *smc5-2KE* mutant, compared to WT, by factors of 1.36, 1.18 and 1.07 for
148 distance 11, 90 and 730 kb from CEN IV, respectively (**Figure supplement 3C**). Increased
149 chromatin mobility of the *smc5-2KE* mutant was verified for another locus located at 90 kb
150 from CEN V (**Figure supplement 3D**) and observed at different phases of the cell cycle,
151 including G1 and metaphase (**Figure supplement 4**).

152 Since lysine residues undergo a wide range of reversible PTMs such as SUMOylation,
153 acetylation and ubiquitination, which can regulate protein functions, including protein-
154 protein interactions (Wang and Cole, 2020), we mutated both lysines to arginine (a positively
155 charged amino acid unaffected by PTM), to determine whether lysine PTMs are involved in
156 the Smc5 effect on chromatin mobility. The *smc5-2KR* mutant showed chromatin mobility like
157 WT (**Figure supplement 3D**) indicating that the positive charges at amino-acid positions 624

158 and 631 of Smc5, rather than their potential to be modified by PTMs, are required to promote
159 normal chromatin dynamics *in vivo*.

160 Finally, since sister chromatid cohesion has been shown to restrict chromatin dynamics during
161 S phase (Cheblal et al., 2020; Dion et al., 2013), we investigated whether cohesion defects in
162 the *smc5-2KE* mutant could account for the observed changes in chromatin dynamics. To do
163 so, we analysed TetO-TetR-GFP at 11 kb from CENIV in mitotically synchronized cells. We
164 analysed the state of sister chromatid cohesion by quantifying the number of cells displaying
165 either one GFP focus (cohesive chromatin) or two GFP foci (defective cohesion) (Garcia-Luis
166 et al., 2022; Paldi et al., 2020). Our analysis revealed no significant differences in the number
167 of cells with single GFP foci between the *smc5-2KE* mutant and the WT strain (**Figure**
168 **supplement 2E**), indicating no cohesion defects. In contrast, the deletion of the Smc1 cohesin
169 subunit, used as a control for defective cohesion, resulted in the separation of GFP foci (**Figure**
170 **supplement 2F**) (Garcia-Luis et al., 2022).

171 Altogether, our results support the hypothesis that lysines K624 and K631, conserved in the
172 C domain of Smc5 hinge, limit chromatin dynamics possibly through the attraction of their
173 positive charge to microtubules, as observed *in vitro*.

174 Increased chromatin dynamics of the *smc5-2KE* mutant is not linked to spontaneous DNA
175 damage or loss of Smc5/6

176 Increase in chromatin dynamics is part of the DNA Damage Response (García Fernández et al.,
177 2022b; Hauer and Gasser, 2017). To determine whether increased chromatin mobility of the
178 *smc5-2KE* mutant results from spontaneous DNA damage, we first monitored Rad52 foci, as
179 a marker of DNA repair at sites of damage (Lisby et al., 2001). While treatment with the
180 genotoxic agent Zeocin yielded a similarly high number of Rad52 foci in WT and *smc5-2KE*
181 mutant (74% ± 6.7 and 79,5% ± 7.8 foci respectively), we observed comparable low levels of
182 Rad52 foci in WT and *smc5-2KE* strains in the absence of Zeocin (7% ± 1.1 and 8.9% ± 1.3 foci
183 respectively) (**Figure supplement 5A**). We also analyzed Rad53 phosphorylation, a checkpoint
184 modification induced by DNA damage (Pellicioli et al., 1999). Rad53 phosphorylation was not
185 detected in *smc5-2KE* cells in the absence of Zeocin, in contrast to Zeocin-treated WT and
186 mutant cells (**Figure supplement 5B**). Finally, we investigated the phosphorylation of histone

187 H2A (γH2A), a conserved PTM induced by DNA damage (Shroff et al., 2004). Upon Zeocin
188 treatment, WT and *smc5-2KE* cells displayed increased levels of γH2A, while γH2A background
189 levels were similar in untreated strains (**Figure supplement 5C**). These observations are
190 consistent with the lack of Rad53 phosphorylation and γH2A observed upon Smc5/6 complex
191 degradation (Peng et al., 2018). Taken together these results establish that the increased
192 chromatin dynamics observed in the *smc5-2KE* mutant are not due to higher levels of
193 spontaneous DNA damage.

194 K624E and K631E mutations do not affect the stability of Smc5/6 *in vitro* (**Figure 1D**), but we
195 could not exclude that a defect in the Smc5/6 complex, undetectable *in vitro*, could account
196 for the increased chromatin mobility of the *smc5-2KE* mutant *in vivo*. To address this point,
197 we investigated chromatin mobility in cells defective for Smc5/6 by specifically degrading
198 Smc5 or Smc6 proteins using the auxin-inducible degron (AID) strategy. Cells expressing AID-
199 tagged Smc5 or Smc6 proteins grew like WT cells in the absence of auxin but failed to grow in
200 the presence of 1 mM auxin (**Figure supplement 6A-B**). This indicates efficient degradation of
201 the tagged proteins and confirms that complete loss of Smc5 and Smc6 proteins is
202 incompatible with cell viability, unlike the separation-of-function phenotype of the *smc5-2KE*
203 mutant. Degradation took place 30 minutes after auxin addition, as shown by western blot
204 for Smc5-AID (**Figure supplement 6C**). Surprisingly, a reduction in chromatin dynamics in the
205 pericentromeric region, at 11 kb from the centromere, was observed when Smc5-AID or
206 Smc6-AID protein degradation was induced by 1h auxin addition (**Figure supplement 6D,F**).
207 These findings contrast with the increase in chromatin dynamics we observed upon
208 degradation of the Smc1 subunit of cohesin (**Figure supplement 6E,F**), as previously
209 documented (Cheblal et al., 2020; Verdaasdonk et al., 2013). The opposite effects of Smc5/6
210 and cohesins on chromatin mobility suggest different mechanisms, which in the case of
211 cohesins might depend on their loop extrusion activity (Costantino et al., 2020; Dauban et al.,
212 2020). Taken together, these results establish that Smc5/6 is required in maintaining
213 chromatin dynamics which is itself constrained by the association of Smc5 with microtubules.

214 The binding of microtubules to kinetochores is necessary but not sufficient to control
215 pericentromeric chromatin dynamics

216 The constraint of pericentromeric chromatin dynamics is in line with studies in budding yeast,
217 showing that release of centromeres from their attachment to the SPB upon microtubule
218 depolymerization or centromere inactivation leads to enhanced chromatin mobility (Amitai
219 et al., 2017; Marshall et al., 1997; Strecker et al., 2016; Verdaasdonk et al., 2013). We
220 therefore investigated chromatin mobility following microtubule depolymerization by
221 nocodazole in WT and in the *smc5-2KE* mutant. We exposed cells to a short treatment (30
222 minutes) with nocodazole (**Figure 2A**) and analyzed chromatin dynamics at different
223 chromosome locations. This treatment depolymerized microtubules, as confirmed by the
224 absence of microtubule filaments visualized by Tub2-GFP (**Figure 2B**) but did not block cycling
225 of the cells (**Figure 2C**). In WT cells, chromatin mobility increased upon exposure to
226 nocodazole at loci far from the centromere, *i.e.* at 90 kb and 730 kb from the centromere, as
227 previously observed (**Figure 2D,G**) (Amitai et al., 2017; Marshall et al., 1997). In contrast, in
228 the *smc5-2KE* mutant, nocodazole had no significant effect on chromatin mobility, indicating
229 that the lack of microtubules or the Smc5-2KE mutation leads to a similar increase in
230 chromosome dynamics with no cumulative effect of the two. Close to the centromere at 11kb
231 from CEN IV, the increase in chromatin dynamics caused by nocodazole nevertheless reached
232 a lower level than that observed in the *smc5-2KE* mutant (MSD_{10s} compared to WT, 1.14 vs.
233 1.32 respectively**, Figure 2D**). These observations support the view that binding of
234 microtubules to Smc5/6 limits chromatin mobility throughout the chromosome and that in
235 the pericentromeric region, Smc5/6 plays an additional role, possibly affecting chromatin
236 properties.

237 In a complementary approach, we analyzed chromatin dynamics in two kinetochore
238 thermosensitive mutants *ndc80*-1, which impairs kinetochores-microtubules binding (Wigge
239 and Kilmartin, 2001) and *ndc10*-1, which affects centromeric chromatin binding (Lechner and
240 Carbon, 1991). To effectively compare these mutants to *smc5-2KE*, we first confirmed that
241 the chromatin behavior reported in the *smc5-2KE* mutant at 30°C is also observed at 37°C,
242 the restrictive temperature for these mutants. Chromatin dynamics at 90 kb from CEN V
243 displayed a comparable increase between *ndc80-1* and *smc5-2KE* single mutants at 37°C
244 (**Figure 2E left, F**), with no additive effect in the *ndc80-1 smc5-2KE* double mutant (**Figure 2E**
245 **left, F**). Conversely, the *ndc10-1* mutant showed no increase in chromatin dynamics compared
246 to the WT, and an increase in chromatin mobility when combined with the Smc5-2KE

247 mutation (**Figure 2E right, F**). These results indicate that only kinetochore mutations
248 disrupting microtubule binding and not chromatin binding have an impact on chromatin
249 dynamics.

250 Our analysis collectively demonstrates that changes in microtubule binding, whether due to
251 KE mutations in the hinge of Smc5, kinetochore mutants that impair binding with
252 microtubules or microtubule depolymerization, are sufficient to enhance chromatin dynamics
253 away from the centromere. They also indicate that Smc5/6 plays an additional role controlling
254 pericentromeric dynamics through its binding to microtubules.

255 The *smc5-2KE* mutant modifies pericentromeric chromatin properties

256 The results above suggested that *smc5-2KE* mutant may impact chromatin properties at
257 pericentromeres. We therefore compared intra-chromosomal distances of different loci in
258 WT and mutant cells. Changes in intra-chromosomal distances underline changes in
259 compaction, rigidity or loop extrusion activity (Hauer et al., 2017; Herbert et al., 2017; Phipps
260 et al., 2024). We used strains R1 and R3 where pairs of differently fluorescently labelled loci,
261 distant by ~180 kb, are scattered on chromosome IV (Herbert et al., 2017) (Material and
262 methods). The R1 strain has two labelled loci, one in in a pericentromeric position (at 4 kb
263 from CEN IV) and one outside (**Figure 3A**) and the R3 strain has two labelled loci located
264 centrally on the chromosome arm (at 735 kb from CEN IV, **Figure 3B**). The *smc5-2KE* mutation
265 was introduced in both strains, and 2D distances between pairs of loci were measured from
266 3D images (Material and methods). As a control, we used Zeocin, which promotes an increase
267 in intra-chromosomal distances at all positions, as previously shown (**Figure 3A,B**) (Hauer et
268 al., 2017; Herbert et al., 2017). While intra-chromosomal distances between pair of loci in R3
269 strain remained similar between R3 WT and R3 *smc5-2KE* strains (**Figure 3B**), a significant
270 increase in intra-chromosomal distances was observed in the R1 *smc5-2KE* mutant compared
271 to the R1 WT strain (**Figure 3A**). This increase suggests that at this sub-chromosomal scale,
272 changes in chromatin properties occur in the *smc5-2KE* mutant, which are revealed when at
273 least one locus is pericentromeric. Although these data do not precisely define whether
274 chromatin decompaction or stiffening are induced by the *smc5-2KE* mutant, they do indicate
275 that the K624 and K631 dependent association of Smc5 with microtubules is required to
276 establish or maintain pericentromeric chromatin.

277 Polymer model recapitulates changes in chromatin dynamics at pericentromeres

278 We next used biophysical polymer simulations (Material and methods) to determine if in the
279 pericentromeric region, microtubule binding and chromatin structure together could drive
280 chromatin dynamics. Initially, we assessed chromatin mobility at positions corresponding to
281 11, 23, 90 and 730 kb from the centromere of different chromosomes. Polymer simulation
282 showed that the increase of MSD_{10s} was proportional to the distance to the centromere as
283 observed *in vivo* and plateaued at 90 kb (**Figure 4A** compared to **Figure 1C**). Although the
284 increase in mobility in the polymer model was less pronounced than in the experimental data,
285 the relative features were present and would allow investigation of the effects of
286 perturbations.

287 We then modified variables related to microtubule tethering and chromatin stiffness and
288 analyzed simulated chromatin dynamics. We first investigated the effect of weakening
289 microtubule tethering to the kinetochore. The spring constant of the harmonic bond between
290 the centromere and the SPB was loosened from a value ensuring a fixed bond to one yielding
291 an energy of 1kbT at 105 nm extension from the 400 nm rest length. Loosening the
292 attachment increased mobility for loci 11 kb away from the centromere, as we observed when
293 microtubules were depolymerized by nocodazole, but left loci 90 kb unchanged **(Figure 2D,**
294 **Figure 4B** - **Figure supplement 7**), indicating that tethering by microtubules induces only a
295 local effect on chromatin mobility (see discussion). We then modified chromatin state by
296 increasing global chromatin stiffness. In contrast to the position-dependent change when
297 weakening microtubule tethering, this led to a global mobility increase independent of the
298 distance from the centromere (**Figure 4C - Figure supplement 8**). This is expected, as even in
299 the simple Rouse model, mobility increases when the spring constant between monomers
300 increases (Herbert et al., 2017).

301 We reasoned that both effects could be at play in the pericentromeric region since the Smc5-
302 2KE mutation displayed a greater increase in mobility than the nocodazole treatment. To test
303 if this was possible, we combined a stiffness increase with the loosened chromatin tethering
304 to microtubules. We observed that stiffening further increased chromatin dynamics, like the
305 results seen *in vivo* for the difference between WT nocodazole and the *smc5-2KE* mutant
306 (**Figure 2D, Figure 4D - Figure supplement 9**). These results show that a relaxation of

307 microtubule attachment and a stiffer chromatin are sufficient to explain the increase in
308 pericentromeric chromatin dynamics observed *in vivo* in the *smc5-2KE* mutant. They further
309 support our hypothesis that Smc5 binds to both microtubules and chromatin to maintain
310 pericentromeric chromatin folding and dynamics.

311 ## The *smc5-2KE* mutant alters the mitotic spindle integrity

312 A correlation between pericentromeric chromatin compaction and spindle elongation has
313 been reported previously, both in yeast and mammals (Bouck and Bloom, 2007; Mora-
314 Bermúdez et al., 2007; Stephens et al., 2011). Since our results point to a role of the
315 association between the Smc5/6 and microtubules on the dynamics and properties of
316 pericentromeric chromatin, this prompted us to investigate spindle elongation. We first
317 studied spindle length by measuring the distance between each spindle pole body (SPB) in
318 dividing G2/M cells. We used SPB protein Spc42 fused to mCherry (He et al., 2000) to calculate
319 the 2D distances between the two fluorescent centers of mass as above (**Figure 3, Figure 5A**
320 **left**). In WT cells, spindle length average was 1.18 ± 0.29 µm, whereas *smc5-2KE* mutant
321 exhibited a significant increase to 1.32 ± 0.33 µm (p value < 0,0001) (**Figure 5A left**),
322 suggesting that the binding between Smc5 and microtubules contributes to the regulation of
323 the spindle length.

324 Alterations in spindle length can arise from changes in the length of the kinetochore
325 microtubules connecting centromeres to the SPB, or modifications in the
326 kinetochore/pericentromere itself. Measuring the distance between GFP-tagged CEN IV and
327 Spc42-mCherry showed no difference between the WT and *smc5-2KE* mutant (**Figure 5A**
328 **right**), suggesting that *smc5-2KE* does not alter the kinetochore microtubules length, while
329 Zeocin control increased CEN-SPB distance as already demonstrated (**Figure 5A right**) (Hauer
330 et al., 2017; Herbert et al., 2017). To then evaluate the kinetochore integrity in the *smc5-2KE*
331 mutant, we measured centromere clustering *in vivo* by visualizing kinetochore protein Mtw1
332 fused to 3xGFP at the endogenous locus (Strecker et al., 2016). Mtw1 is a kinetochore-specific
333 protein, part of the MIND complex, which links the inner and outer layers of the kinetochore
334 (Maskell et al., 2010). While Mtw1-3xGFP expressing cells cycled normally, combination with
335 *smc5-2KE* surprisingly led to a mitosis defect reminiscent of the no-cut phenotype, where
336 completion of cytokinesis is delayed (**Figure 5B right**) (Norden et al., 2006). Strikingly, deletion

337 of Mad2 or bub1, key spindle assembly checkpoint (*SAC*) components, suppressed the mitotic
338 defect we observed, allowing cells to progress through mitosis despite the presence of the
339 *Smc5-2KE* mutation and *Mtw1-3xGFP* (**Figure 5B right**).

340 In WT cells, Mtw1-3xGFP formed a single fluorescent focus due to the centromeric clustering
341 typical of the Rabl configuration. Treatment with the microtubule-depolymerizing drug
342 nocodazole induced fragmentation of the Mtw1-3xGFP labelling into several foci, consistent
343 with centromeres declustering, as previously reported (Richmond et al., 2013; Strecker et al.,
344 2016). Strikingly, when compared to WT, the *smc5-2KE* mutant presented a high percentage
345 of cells with centromere declustering (27.26 ± 4.3% and 9.89 ± 2.5% for *smc5-2KE* and WT
346 cells respectively, **Figure 5C**).

347 Overall, our results indicate that *smc5-2KE*, in the presence of Mtw1-3xGFP hypomorphic
348 allele, exacerbates a kinetochore defect that activates the SAC. It suggests that the molecular
349 link between chromatin and microtubules provided by Smc5/6 participates in kinetochore
350 maintenance and mitotic spindle integrity.

351 The *smc5-2KE* mutant affects homologous recombination at pericentromeres

352 To investigate whether Smc5/6 microtubule-dependent pericentromeric folding is required
353 for genomic integrity, we induced targeted unique DSB in the pericentromere or far from it
354 and analyzed its efficiency of repair by HR or NHEJ both in WT and mutated smc5-2KE strains
355 according to (García Fernández et al., 2022a, 2021) (**Figure 6A**). I-*Sce*I is expressed on a
356 plasmid with the galactose-inducible *GAL1-10* promoter to induce the DSB (+DSB), while an
357 empty vector serves as control (-DSB). In the presence of a donor, successful HR leads to
358 mCherry expression, detectable by red fluorescence in living cells (**Figure 6A**). Recipient
359 sequence was introduced at 5 kb (named C) and 404 kb (named L) from CEN IV in both the
360 WT and the *smc5-2KE* mutant strains, resulting in four distinct strains (**Figure 6B**). The I-*Sce*I
361 cleavage efficiency in these strains, quantified by qPCR, was ~80%, after 6 hours of I-*Sce*I
362 induction, irrespective of the position of the cutting site, as previously observed (García
363 Fernández et al., 2022a) (**Figure supplement 10A**). Cell survival was assessed by colony
364 forming unit (CFU) assays. As expected, in the absence of I-*Sce*I, WT and *smc5-2KE* C and L
365 colonies grew in both inducing and non-inducing conditions (**Figure 6B**).

366 Interestingly, providing the donor sequence on the dCEN plasmid to allow DSB repair by HR,
367 had different outcomes in *smc5-2KE* depending on the DSB position. When the DSB was in
368 the pericentromeric region, the *smc5-2KE* mutant showed significantly reduced survival rates
369 compared to the WT (C strains, 15 ± 6% and 55 ± 12.4%, respectively, **Figure 6B**). In contrast,
370 both WT and the *smc5-2KE* mutant presented similar survival rates for a DSB located in the L
371 position (40 ± 7.5% for both L strains) (**Figure 6B**). The smc5-2KE mutant generated fewer
372 mCherry-positive cells than the WT at the pericentromeric DSB (WT, 44 ± 3.4% and *smc5-2KE*
373 22.5 ± 1.7%. Importantly, at the L position, both WT and smc5-2KE strains showed comparable
374 mCherry expression levels (36 ± 2.5% for both). HR defect could not be explained by a loss of
375 the centromeric plasmid (**Figure supplement 10B**) nor a change in Smc5/6 occupancy at DSB,
376 as ChIP-qPCR of Smc5-MYC or *smc5-2KE*-MYC revealed no significant differences, irrespective
377 of the DSB position (**Figure supplement 10C-D**).

378 Overall, these results indicate that *smc5-2KE* impairs HR at pericentromeres, but not along
379 the chromosome arm, and suggest that pericentromeric folding due to Smc5 binding to
380 microtubules is required for pericentromeric integrity.

381 Local mobility induced by a DSB is facilitated by microtubules (Lawrimore et al., 2017; Oshidari
382 et al ., 2018) and has been proposed to promote DSB repair by HR (Miné-Hattab et al., 2017;
383 Neumann et al., 2012). We therefore analyzed chromatin mobility at the DSB in the *smc5-2KE*
384 mutant. We introduced a lacO-LacI-GFP array at 10 kb away from the I-*Sce*I cutting site in WT
385 and mutant C and L strains and verified by qPCR that the efficiency of I-*Sce*I cutting was not
386 affected by the array in all strains (80% at 6 hours after induction) (**Figure supplement 10E**).
387 Chromatin dynamics was tracked after 6 hours of induction, and MSD was plotted through
388 increasing time intervals (**Figure supplement 10F-G**). DSB induction in WT led to an increase
389 in chromatin dynamics, independently of the DSB position, whereas in the *smc5-2KE* mutant,
390 DNA damage did not cause an additional increase in mobility on top of the one generated by
391 the mutation, as reported above (**Figure 1 -figure supplement 10F-G**). These results show that
392 differences in HR efficiency between a pericentromeric DSB and a mid-arm DSB are not
393 related to changes in local chromatin dynamics and suggest that Smc5-microtubule
394 association is required for a fraction of the mobility induced by a DSB.

395 ## Discussion

396 Pericentromeres across eukaryotic evolution are enriched with SMC complexes, which share
397 the conserved role of extruding DNA to create loops (Davidson et al., 2019; Ganji et al., 2018;
398 Pradhan et al., 2023). The pericentromeric enrichment of SMCs and their extruding activity
399 theoretically leads to a structure described, from a physical perspective, as a bottlebrush,
400 balancing the outward pulling forces of microtubule with the inward attractive forces of
401 chromatin during cell division (Bloom, 2024). Smc5/6 has been shown to associate with
402 microtubules in budding yeast and *Xenopus* (Gache et al., 2010; Gutierrez-Escribano et al., 2020;
403 Laflamme et al., 2014 and our present data - **Figure supplement 1**). However, the role of this
404 association in organizing pericentromeric structure *in vivo* was previously unknown. By
405 measuring chromatin dynamics in the *smc5-2KE* mutant, which decreases the affinity between
406 Smc5 and microtubules, we demonstrate that Smc5 associates with microtubules *in vivo* and
407 regulates chromatin mobility along the chromosome, as well as chromatin properties in the
408 pericentromeric region. Moreover, we show that Smc5/6 association with microtubules
409 specifically maintains the integrity of the mitotic spindle and contributes to DSB repair
410 efficiency in the pericentromeric region.

411 We provide evidence that Smc5/6 offers a molecular link to microtubules through the
412 conserved residues K624 and K631 in the hinge region of Smc5. First, alphafold3 modelling
413 shows a high probability of interaction between extruded Smc5 hinge and alpha/beta dimers of
414 tubulin (**Fig 1A**). Second, the microtubule binding co-sedimentation assay with Smc5 is
415 decreased when K624 and K631 are mutated to aspartic acid (**Figure 1C**). Third, in the *smc5-2KE*
416 mutant, chromatin dynamics mirrors microtubule depolymerization (**Figure 2D,F**) and
417 resembles the effects observed in the *ndc80-1* kinetochore mutant (**Figure 2E,F**). The ability of
418 Smc5/6 to bind microtubules is thus an important emerging property of this complex.

419 The association between Smc5/6 and microtubules restricts chromatin mobility and has
420 critical consequences for the folding of the pericentromeric region. In this region,
421 measurements of both chromatin mobility and intra-chromosomal distances in the *smc5-2KE*
422 mutant indicate that reduced association with microtubules, and only them, impacts
423 chromatin structure, potentially leading to increased rigidity or decompaction, as shown by
424 polymer modelling (**Figure 4D**). Notably, changes in nuclear environment (i.e. changes in
425 chromatin density because of centromere release in a configuration where centromeres are

426 clustered due to Rabl configuration) are consistent with an increased chromatin mobility with
427 similar alpha exponent of the MSD **(Fig 1E).** How could the Smc5-2KE mutation affect the
428 properties of pericentromeric chromatin? Loss of microtubules polymerization or kinetochore
429 mutants, such as Gal-Nuf2, where Nuf2 is repressed in the presence of glucose, result in
430 decreased levels of histone H4 and H2B in the pericentromere, as shown by FRAP
431 (Verdaasdonk et al., 2012). Because histone reduction has been linked to chromatin
432 decompaction and increased chromatin dynamics (Amitai et al., 2017; Cheblal et al., 2020;
433 Hauer et al., 2017), disruption of microtubule-induced tension in the *smc5-2KE* mutant could
434 similarly result in decreased histones occupancy, chromatin decompaction and subsequent
435 chromatin mobility increase. The fact that the loss of microtubules also increases intra-
436 chromosomal contacts and affects pericentromeric configuration (Paldi et al., 2020), suggest
437 that the tension created by microtubules can regulate chromatin structure close to the
438 attachment sites (Paldi et al., 2020). Accordingly, the interaction between Smc5 and
439 microtubules, disrupted in the *smc5-2KE*, may contribute to microtubule-induced tension and
440 spindle robustness, thereby influencing pericentromeric chromatin architecture.

441 Another interesting possibility by which Smc5/6 might regulate pericentromeric chromatin
442 structure could be via its DNA compaction activity, as recently shown by single molecule
443 experiments with purified human and yeast Smc5/6 (Gutierrez-Escribano et al., 2020; Serrano
444 et al., 2020). Mechanistically, the altered chromatin structure in the *smc5-2KE* mutant could
445 result from impaired loop extrusion by Smc5/6 dimers (Pradhan et al., 2023). However, we
446 show here that acute depletion of the entire complex - thereby abolishing loop extrusion
447 activity - has an impact on chromatin mobility opposite to the Smc5-2KE mutation (**Figure**
448 **supplement 6)**. This finding strongly suggests that loop extrusion is not responsible for the
449 altered chromatin behavior in *smc5-2KE.* Instead, Smc5/6 could promote chromatin
450 compaction through alternative mechanisms, such as microtubule-associated nucleosome
451 stabilization. Defects in cohesin or condensin recruitment could also contribute to
452 pericentromeric decompactionr or stiffness leading to increased chromatin dynamics (**Figure**
453 **1C**) (Cheblal et al., 2020; Dion et al., 2013; Verdaasdonk et al., 2013). Pairing defects by
454 cohesin appear unlikely in the *smc5-2KE* mutant, as cohesion is intact, contrasting what is
455 observed upon cohesin-depleted cells (**Figure supplement 6D,E).** Overall, our observations

456 suggest a pathway in which microtubule forces transmitted via Smc5/6 regulate
457 pericentromeric chromatin folding and stiffness, independently of loop extrusion or cohesion.

458 It is intriguing that disrupting the microtubule binding to centromeres, either by
459 depolymerization of microtubules in the presence of nocodazole, by affecting the kinetochore
460 in the *ndc80-1* mutant or with the *smc5-2KE* mutant results in increased chromatin dynamics
461 not only close to the centromere but also, to a lesser extent, at locations distant from it. It is
462 possible that once centromeres are freed from microtubules, they exhibit increased
463 movement, which could be translated into greater chromatin mobility further along the
464 chromosome. By analogy, a rope with movement at one end could lead to increased
465 movement at the other end. However, by simulating weakened microtubule anchoring, the
466 polymer model fails to fully reproduce the *in vivo* increase in chromatin dynamics away from
467 the centromere (**Figure 4B**), possibly due to unmodeled features such as SMC-mediated loop
468 formation or centromeres declustering, which might influence chromatin density *in vivo.*

469 One of the pericentromeric chromatin functions mediated by the association of the Smc5/6
470 complex with microtubules is clarified by the "no-cut" phenotype (**Figure 5B**). Defects in
471 cytokinesis are indeed observed when the *smc5-2KE* mutant is combined with Mtw1-3xGFP.
472 This phenotype, also described in cells with mutations in kinetochore proteins such as *ndc10-*
473 *1* and *ndc80-1* alleles (Bouck and Bloom, 2005; Norden et al., 2006) suggests that the
474 interaction between the Smc5-2KE mutation and Mtw1-3xGFP is associated with
475 compromised kinetochores (Fujioka et al., 2002). The “no-cut” phenotype has been described
476 in cells with incomplete DNA segregation (Mendoza et al., 2009), indicating that disruption in
477 chromosome segregation can lead to cytokinesis defects. Strikingly, deletion of *Mad2* or *Bub1*
478 suppressed the mitotic defect, indicating that the no-cut phenotype is SAC-dependent and
479 further supports the hypothesis that Smc5-2KE and Mtw1-GFP exacerbate kinetochore
480 dysfunction to a degree that activates the SAC. Thus, it is conceivable that the combination of
481 Smc5-2KE with Mtw1-3xGFP results in chromosome segregation defects leading to the “no-
482 cut” phenotype and pinpoints to the important function of Smc5/6 in establishing
483 pericentromeric chromatin through its association with microtubules.

484 It has previously been shown both in budding yeast and mammalian cells, that Smc5/6 is
485 enriched around DSBs (De Piccoli et al., 2006; Lindroos et al., 2006; Potts et al., 2006) and

486 contributes to HR by resolving Holliday junctions (Bermúdez-López et al., 2010; Pebernard et
487 al., 2006; Torres-Rosell et al., 2005), as well as by maintaining the ends of a DSB together
488 (Phipps et al., 2024). In line with the role of Smc5/6 in HR, we show that the Smc5-2KE
489 mutation leads to reduced repair efficiency only at pericentromeres (**Figure 6**). HR efficiency
490 could be impacted either because pericentromeric chromatin properties are modified as we
491 observed due to the lack of association between Smc5/6 and microtubules (**Figure 3**), or
492 because *smc5-2KE* mutant directly impairs pericentromeric DSB repair. For instance, mutating
493 the hinge domain of Smc5, which has been shown to have affinity for ssDNA *in vitro* (Alt et
494 al., 2017; Roy et al., 2011), could affect the putative interaction between the Smc5/6 complex
495 and ssDNA at DSB, potentially impacting 5' DNA resection at DSBs or the maintenance of the
496 DSB ends (Phipps et al., 2024). Alternatively, the lack of association between microtubules
497 and the Smc5/6 could hinder the efficient relocalization of damaged pericentromeres to the
498 nuclear periphery, in line with the reported role of the Smc5/6 complex relocalization for DSBs
499 in repetitive rDNA sequences in budding yeast (Torres-Rosell et al., 2007) and in
500 heterochromatin in *Drosophila* (Caridi et al., 2018; Ryu et al., 2015). Furthermore, upon a DSB
501 near the centromere, DNA resection may lead to detachment of the centromere from
502 microtubules, triggering the formation of damage-induced microtubules (DIM) to recapture
503 the centromere as proposed (Oshidari et al., 2018). This process would require Smc5/6; thus,
504 a mutation affecting association with DIMs could hamper centromere recapture and efficient
505 DSB repair. These alternatives explanation deserve further investigation in future studies.

506 Taken together, our focus on chromatin dynamics emerged as a powerful approach for
507 understanding the functional relevance of the association between Smc5/6 with microtubules
508 on the maintenance and integrity of pericentromeric chromatin. We propose that the
509 enrichment of Smc5/6 at pericentromeres, together with its association with microtubules,
510 contribute to the maintenance of pericentromere chromatin stability in the face of mitotic
511 forces. Smc5/6 enrichment in the pericentromeric region is conserved throughout mitosis of
512 many organisms (Jeppsson et al., 2014; Lindroos et al., 2006; Venegas et al., 2020). It is likely
513 that a similar association between Smc5/6 and microtubules occurs in mammals during open
514 mitosis, the only phase when microtubules interact with centromeric regions in mammals.
515 Therefore, the role of Smc5/6 in preserving pericentromeric structure during mitosis might
516 be conserved through evolution.

517 # Material and methods

518 ## Yeast strains

519 *S. cerevisiae* strains used in this study are detailed in **Table 1** and isogenic to BY4741.

520 ## Strain construction

521 Mutations of K624E and K631E of *SMC5* were performed with CRISPR/Cas9 using a 80 pb
522 donor carrying the desired mutations as described in (García Fernández et al., 2022a). Unique
523 duplexed 20 nucleotides long primers next to the PAM sequence (AGG) close to K631
524 (oACS13/14) were cloned into a replicative Cas9-KANMX plasmid (pEF562, Addgene plasmid
525 #100955) to yield (pEF590) verified by PCR and sequencing. Equimolar amounts of pEF590
526 and the 80 pb donor (oACS69) were used to transform the desired strains and the
527 corresponding smc5-2KE transformants were verified by sequencing. The same strategy was
528 used to obtain smc5-2KA and smc5-2KR with different donor sequences carrying the specific
529 mutation (oACS97 and oACS270 respectively).

530 The strains used to track the local mobility of a DSB were constructed as described in (García
531 Fernández et al., 2022a). Briefly, the I-*Sce*I cutting site was inserted at the desired position,
532 by replacing a KANMX cassette integrated into intergenic regions of chromosome IV at
533 positions 453880-453959 (C strain) or 853996-854075 (L strain) with an mCherry sequence
534 containing the I-*Sce*I cutting site. LacO repeats at 10 kb from the cutting site were introduced
535 by replacing a KANMX cassette integrated at positions 462252-462602 (strain C) or 844554-
536 844952 (strain L) with pEF222 plasmid digested by *Bgl*II (BioLabs, R0144). LacI-GFP was
537 introduced by digesting plasmid pEF569 (Therizols et al., 2010) with *Nhe*I (BioLabs, R3131).
538 The ARS-CEN-HIS3 plasmid (pB07, obtained from B. Pardo) for I-*Sce*I expression under
539 inducible pGAL1-10 promoter, was used after insertion of a stop codon in the *HIS3* genomic
540 sequence by CrispR/Cas9 as above. The 20 nucleotides duplex oligos (oACS204/205) next to
541 the PAM (TGG) sequence in *HIS3* and an 80 pb primer (oACS208) donor were used.

542 Depletion of *SMC5* was obtained by using a degron AFB2 based inducible (Nishimura and
543 Kanemaki, 2014). AID-9MYC tag at the C-terminus of *SMC5* was introduced by homologous
544 recombination using pEF565 (Morawska and Ulrich, 2013) and (oACS40/53) oligonucleotides.

545 AFB2 was introduced at the *HIS3* locus by digesting the plasmid pEF604 (obtained from
546 T.Teixeira) carrying *AFB2-HIS3* by *Nhe*I (BioLabs, R3131).

547 ## Media and growth conditions

548 Cells were grown in SC medium (2 g/l amino acids mix, 20 g/l sugar, 6.7 g/l yeast nitrogen
549 base) until they reached the mid-log phase. Multiple DNA damages were induced with 250
550 µg/ml Zeocin (Thermo Fisher, R25001) added for 4 hours (Herbert et al., 2017). Microtubules
551 were depolymerized using 15 ng/µl of nocodazole (Sigma, M1404) dissolved in DMSO, for 30
552 minutes. Depolymerization was checked in parallel by Tub1-GFP disappearance in strain
553 YPT257 (Therizols et al., 2010). To induce a single DSB, 2% of galactose was added for 6 hours.

554 G1 arrest was performed using 50 ng/ml of alpha-factor (Zymo Research, Y1001M) in *Δbar1*
555 deleted strains during 3 hours prior to imaging. G2/M arrest in metaphase was done through
556 P_{MET3}-*CDC20* (Paldi et al., 2020) depletion with 2 mM methionine added 2 hours before
557 imaging. G2/M arrest in prometaphase was performed with nocodazole (Sigma, M1404), 20
558 ng/µl during 1h and 10 ng/µl for an additional hour. Smc5, Smc6 or Smc1 degradation was
559 obtained by adding 1mM of auxin (Sigma, I3750-5G-A), dissolved in Ethanol 100%, 1 hour to
560 the culture before imaging.

561 ## Mass spectrometry

562 Purification of the endogenous yeast Smc5/6 complex was performed as described in
563 (Adhikary and D'Amours, 2025) with minor modifications. A yeast culture (30L) was grown at
564 30 °C until it reached an OD_{600} of 0.7 – 1.0 and then further incubated at 18 °C for 16 hrs. Cells
565 were collected and washed with H_2O before being snap frozen. Cells were subsequently
566 thawed on ice in NBE buffer (50 mM potassium phosphate buffer pH 8, 50 mM Tris-HCl pH 8,
567 500 mM NaCl, 10% glycerol, 0.5% Triton X-100, supplemented with 20 mM imidazole, 2 mM
568 ß Mercapto-Ethanol, 2X protease inhibitors, pH 8). Snap frozen droplets of cell suspensions
569 were lysed using a freezer mill. The resulting powder was then resuspended in NBE buffer and
570 cleared by high-speed centrifugation. The cleared lysate was subjected to two consecutive
571 rounds of Ni-NTA purification. The Ni-NTA columns were washed with 10 CV of NW buffer (50
572 mM potassium phosphate buffer pH 8, 50 mM Tris-HCl pH 8, 500 mM NaCl, 10% glycerol, 0.5%
573 Triton X-100, supplemented with 60 mM imidazole, 2 mM ß Mercapto-Ethanol, and protease

574 inhibitors, pH 8) and bond proteins were eluted with 5 CV of buffer NE (50 mM Tris HCl pH 8,
575 500 mM NaCl, 10% glycerol, 0.5% Tween-20, supplemented with 500 mM imidazole, 2 mM
576 bME, and 1X protease inhibitors, pH 8). Eluted fractions were loaded on an SDS-
577 polyacrylamide gel (4–12% Bis-Tris) in 1 x MOPS buffer and ran for 90 mins at 150 volts before
578 being stained with Coomassie Blue. Peak fractions from both columns were combined and
579 loaded on a 5mL Strep-Tactin XT column using an AKTA FPLC purification system. The column
580 was washed with 10 CV of buffer SW (50 mM Tris HCl pH 8, 500 mM NaCl, 10% glycerol, 0.5%
581 Tween-20, 2 mM ß Mercapto-Ethanol, 1X protease inhibitors, supplemented with 0.5% Triton
582 X-100, pH 8) and eluted with 12 CV of STE buffer (150 mM NaCl, 10% glycerol in PBS 1X,
583 supplemented with 50 mM Biotin, 2mM ß Mercapto-Ethanol, 1X protease inhibitors, pH 8).
584 Peak elutions were snap frozen and stored at -80 °C

585 ### MT binding and cell proliferation assays

586 The affinity of Smc5 hinge domain (residues 215 to 885) for MT polymers was monitored using
587 a pelleting assay, as previously published (Laflamme et al., 2014). The proliferation phenotype
588 of cells expressing wild-type and smc5 mutants was assessed by spotting 5-fold dilutions of
589 yeast cultures on the surface of solid medium and monitoring yeast growth at the indicated
590 temperatures after 2-4 days incubation at various temperatures (Laflamme et al., 2014).

591 ### Co-immunoprecipitation (co-IP) of Smc5/6 complex subunits

592 The co-IP was performed as described in (Roy et al., 2024; under revision at eLife) with minor
593 modifications. Yeast cultures (50mL) were grown at 30°C in YEPD medium to an optical density
594 (OD_{600}) of 0.7–0.8. Cells were harvested and lysed with glass beads in co-IP lysis buffer (50mM
595 HEPES – KOH pH 7.5, 140mM NaCl, 1% Triton X-100, 0.1% sodium deoxycholate, 1mM EDTA
596 pH 8.0, 1mM AEBSF, 10µM Pepstatin-A, 10µM E64). The purification resin (StrepTactin XT®)
597 was washed with sterile water and PBS-BSA buffer (1x PBS [phosphate buffered saline], 1%
598 BSA) just prior to the co-IP experiment. Cell lysates were cleared by centrifugation (30 minutes
599 at 13,000rpm) and combined (1mL) with the washed resin for an overnight incubation (~12h)
600 at 4°C with gentle rotation (20rpm). The resin was subsequently washed in sequence with 1)
601 co-IP lysis buffer, 2) high salt buffer (50mM HEPES – KOH pH 7.5, 360mM NaCl, 1% Triton X-
602 100, 0.1% Sodium deoxycholate, 1mM EDTA pH 8.0) and 3) TE buffer (10 mM Tris-HCl pH 8.0,

603 0.1 mM EDTA). The purification resin was finally resuspended in 2X SDS-PAGE sample buffer
604 and heated at 95°C for 5 minutes to elute purified proteins. The eluted proteins were
605 separated on a SDS-polyacrylamide gel [4-12% Bis-Tris gel ran with 1x MOPS electrophoresis
606 buffer (20mM MOPS [3-(N-Morpholino) propanesulfonic acid], 5mM of sodium acetate, 1mM
607 of disodium EDTA [isodium ethylenediaminetetraacetate dihydrate]) for 2h at 120 volts,
608 before being transferred to a membrane and analysed by immunoblotting using a 1:2,000
609 dilution of mouse anti-Strep antibody and 1:5,000 dilution of mouse anti-Myc (9E10) antibody
610 (GeneTex 369661).

611 ### Cell cycle time course experiment

612 To assess the kinetics of cell cycle progression, a time course experiment was performed as
613 previously described (Ratsima et al., 2011). Specifically, yeast strains were grown in YPD
614 medium at 30°C until they reached an OD_{600} of 0.3-0.4. Alpha factor was then added (5µg/mL)
615 to the medium and, after 1h of growth, a second dose (2µg/mL) was added to ensure optimal
616 arrest in G1. Once ≥ 90% of the cells were synchronized in G1, they were released at 30°C in
617 fresh YEPD medium. Alpha factor (5µg/mL) was added 45 minutes after the initial release to
618 prevent cell cycle re-entry after completion of the first mitosis. For each time point, 1.5ml of
619 cells were collected and pelleted for 2 minutes at 3,000rpm. Cells were then fixed in 1mL of
620 70% ethanol overnight at 4°C. Cells were washed twice and resuspended in 0.1M KPO_4 pH7.0
621 buffer. DAPI (4',6- diamidino-2-phenylindole; 2µg/ml) was used to stain yeast nuclei.
622 Separation of nuclei was manually counted in 100 cells per time-point (N=3). Fluorescent
623 images were taken using a Nikon Eclipse Ti2 inverted microscope, with an 100x oil immersion
624 objective.

625 ### Flow cytometry

626 Yeast cells were grown in SC selective medium overnight at 30°C, diluted to $O.D_{600}$ nm = 0.5
627 in 5 ml next morning for 1h30 at 30°C. If necessary, cells were arrested at G1 or G2/M. 10^7
628 cells were centrifuged, fixed in 200 µl 70% ethanol and stored at 4°C for 48h. To perform FACS,
629 cells were centrifuged at 10.000 rpm 5 minutes at 4°C, washed and resuspended in 1 ml of
630 sodium citrate (50mM, pH7). 200 µl cells were transferred in polystyrene round-bottom tubes
631 with 20 µL of RNaseA (10 mg/ml Roche, 10109169001) and incubated 1 h at 37°C. Cells were

632 resuspended in 2 ml of sodium citrate (50mM, pH7) with 2.5 µM of SYTOX™ Green nucleic
633 acid stain (Sigma, S7020). Cells were stained 1h at 4°C in the dark for 1 hour. Cells were and
634 analysed with the Attune NxT Flow cytometer.

635 ## Microscopy

636 For microscopy, cells were grown as for FACS. Cells were plated on agarose patches (made of
637 SC medium containing 2% agarose) and sealed using VaLaP (1/3 Vaseline, 1/3 Lanoline and
638 1/3 Paraffin). Cells were imaged using a widefield microscopy system Nikon Ti-E equipped
639 with the Perfect Focus System (PFS) and a 60x oil immersion objective (Nikon, Plan APO).
640 Andor Neo Scmos camera allowed a vision field of 276x233 µm with a pixel size of 108 nm.
641 Fluorochromes were excited with 35% LED with a wavelength of 477 nm for GFP or 40% LED
642 with a wavelength of 587 nm for mCherry.

643 ## Dynamic analysis

644 Analyses of chromatin mobility were performed as described in Herbert et al., 2017. Briefly,
645 GFP tracking was performed by video microscopy for 3 minutes with an interval time of 100
646 ms in two dimensions (x,y). A Fiji plugin was used to isolate and extract locus trajectory at
647 each time point throughout the film. After drift correction and signal-to-noise ratio checked
648 with MATLAB scripts, Mean square distances (MSDs) for each trajectory were calculated and
649 concatenated. Power laws to the mean MSD of a population over time intervals between 0.1
650 and 10s were adapted with MATLAB script and graphs of averaged MSDs were plotted in
651 linear or log/log.

652 For each single locus trajectory sampled at a time resolution δt for an overall time T, the MSD
653 at time Δt is calculated as the time-average over the $M = \frac{T-\Delta t}{\delta t}$ frames of the squared
654 displacement performed by the locus between a running initial time $m\delta t$ and the increased
655 time $m\delta t + \Delta t$:

656 $$MSD_i(\Delta t) = \frac{1}{M}\sum_{m=1}^{M}\left|\vec{r}_i(m\delta t + \Delta t) - \vec{r}_i(m\delta t)\right|^2,$$

657 For an ensemble of N trajectories (cells), one gets an ensemble of N $MSD_i(\Delta t)$ curves; the
658 index i therefore refers to i-th the trajectory. Each single curve can then be fitted to a $y(\Delta t) =$

659 $D\Delta t^{\alpha}$ function leading to a value of the exponent α. The distribution of the ensemble of the
660 values of α obtained is shown in **Figure 1F**. In principle, the sub-diffusion coefficient D is also
661 obtained by the same fitting procedure. However, we found that an equivalent, but more
662 robust estimate of the sub-diffusion coefficient is obtained by the trend of the MSD over the
663 very first 15 points, as $D = \frac{MSD_i(15\delta t)}{15\delta t}$. The D histograms of **Figure 1F** refer to this definition
664 of the sub-diffusive coefficient.

665 The MSD can also be averaged over the ensemble of N trajectories (cells) as

666 $$MSD(\Delta t) = \frac{1}{N}\sum_{i=1}^{N} MSD_i(\Delta t) = \frac{1}{N}\sum_{i=1}^{N}\frac{1}{M}\sum_{m=1}^{M}\left|\vec{r}_i(m\delta t + \Delta t) - \vec{r}_i(m\delta t)\right|^2,$$

667 corresponding to the curves of **Figure 1E**.

668 ## Distances analysis

669 The analysis of distances between two differently labelled dots (GFP and mCherry) was carried
670 out either for intrachromosomal loci, or for a pericentromeric locus and the SPB. Acquisition
671 of 3D z-stacks consist of 35 frames with z steps of 300 nm, illumination with two consecutive
672 color channels for each plane with an exposure time of 100ms using a dual band filter set.
673 First, using images from a strain dually labelled for the same locus, chromatic aberration was
674 corrected using the plug-in "Descriptor based registration (2d/3d)". The 3D z-stacks were then
675 converted to 2D using a maximum intensity projection. The dots were then selected using Fiji
676 and the (x,y) coordinates of the red and green loci calculated using a home-made script on
677 Fiji, taking into account the Gaussian intensity of each fluorescent loci. Comparison of
678 distances between loci was performed using Wilcoxon rank-sum tests.

679 ## ChIP-qPCR

680 Yeast cells were grown either in YPD medium or SC-His Raff 2% overnight at 30ºC. Next
681 morning, cells were diluted to a O.D_{600} nm of 0,5 in 45 ml and cells were incubated at 30ºC
682 during 1h30 to reach the exponential phase. To check expression of Smc5 in the whole
683 genome, cells were synchronized at G2/M phase using nocodazole (Sigma, M1404,).
684 Nocodazole (cci. 2 mg/mL) was added two times during the time of synchronization, 20 ng/µL
685 during a first 1h at 30ºC and then 10 ng/µl for an additional hour at 30ºC under agitation. Cell

686 cycle arrest was verified by flow cytometry. In order to check the enrichment of Smc5 around
687 the DSB, DSB was induced to the cell cultures by addition of 2% galactose during 6 hours at
688 30ºC. 50 OD were recollected and treated with 1% formaldehyde for 12 minutes at room
689 temperature with rotation. Crosslinking was quenched by using 2,25 mL of glycine 2,5 M for
690 5 minutes with rotation. Then, samples were harvested by centrifugation at 3000 rpm for 5
691 minutes and washed twice with cold TBS 1X.

692 Cells pellet was resuspended in 1,2 ml of lysis buffer (50 mM HEPES-KOH pH7.5, 140 mM NaCl,
693 1 mM EDTA, 1% Triton-X 100, 0.1% sodium deoxycholate) supplemented with 1 mM PMSF,
694 phosphatase inhibitor, anti-protease (Roche, 04693132001) and 300 mg of glass beads
695 (Sigma, G8772) and lysed by MagNA Lyser rotor (Roche, 03359093001). The lysate was
696 obtained by centrifuging an eppendorf tube perforated with a sterile needle at 1000 rpm for
697 1 minute and recovering the extract in a new tube. The extract was transferred to a 1,5 ml
698 falcon tube and sonicated with a PICO sonicator (15x: 30 sec ON, 90 sec OFF, high intensity)
699 to obtain DNA with a range between 200 - 500 pb. After sonication cells were centrifuged for
700 10 minutes at 10.000 rpm at 4ºC and 25 µL of the supernatant was saved at -80ºC as INPUT.
701 250 µL of DNA after sonication were incubated with 1 µL of DNA carrier (ST0029, TakaRa Bio),
702 25 µL of BSA 5% (BP1600, Janssen Pharmacy) and 3,2 µg of anti-MYC antibody (Santa Cruz,
703 Biotechnology, INC) overnight at 4ºC. 30 ml of *Dynabeads™ Pan Mouse IgG* (Thermo Scientific,
704 11041) were added and incubated at 4ºC for 4 hours. Beads were washed twice with lysis
705 buffer, twice with lysis buffer + 0,36 M NaCl (50 mM HEPES-KOH pH7.5, 360 mM NaCl, 1 mM
706 EDTA, 1% Triton-X 100, 0.1% sodium deoxycholate), twice with washing buffer (10 mM Tris-
707 HCl pH8, 0.25 M LiCl, 0.5% NP40, 1 mM EDTA, 0.1% sodium deoxycholate) and once with
708 elution buffer (50 mM Tris-HCl pH8, 10 mM EDTA). The supernatant was removed and the
709 immunoprecipitated chromatin was then eluted by incubation in 250 µL TES buffer (50 Mm
710 Tris-HCl, pH 8.0; 10 mM EDTA; 0,5% SDS) for 15 minutes at 65ºC and the supernatant
711 collected, termed IP. The INPUT was mixed with 120 µl of TES buffer. Both INPUT and IP were
712 de-cross-linked at 65ºC with agitation overnight. RNA was degraded by incubation with 2µL
713 RNase A (10 mg/mL) for 1h at 37ºC. Proteins were removed by incubation with 20µL of
714 proteinase K (10 mg/mL) for 2h at 37ºC. DNA was purified by a phenol/Chloroform extraction.

715 Drop test

716 Overnight cultures were diluted to a $O.D_{600}$=0.5 and cells were incubated at 30ºC until they
717 reached the exponential phase. Serial 1:5 dilutions were plated starting with a O.D.= 0.2 using
718 the replication plate (R2383-1EA, Sigma) on YPD with or without 100nM hydroxyurea (Sigma
719 H8627), 10 μM Camptotehcin (Sigma C9911) and 0.2 μM 4-Nitroquinoline 1-oxide (Sigma
720 N8141). Plates were incubated at 30°C for 72 hours.

721 Colony formation unit (CFU)

722 To quantify the colonies formed in the absence or presence of an I-*Sce*I induced DSB, cells
723 were grown in -Ade -His + raffinose 2% liquid medium overnight at 30°C. After 24 hours, cells
724 were counted in a Malassez chamber and ~ 100 - 200 cells were spread on -Ade – His +
725 glucose (control) or + galactose plates (DSB induction). Plates were incubated at 30°C and
726 colonies were counted after 72h.

727 Plasmid maintenance assay

728 Plasmid stability was assessed using the centromeric plasmid pRS415. WT and smc5-2KE
729 mutant cells carrying the plasmid were grown overnight in YPD 200 cells were spread on YPD
730 and replica plated on SC-Leu plates to determine the fraction of plasmid-retaining cells.
731 Plasmid maintenance efficiency was calculated as the ratio of colony-forming units on SC–Leu
732 versus YPD plates.

733 Western blot

734 Electrophoretic protein separation was done using Bolt™ 4-12% Bis-TrisPlus (Thermo Fisher
735 NW04122BOX) in Mini gels tanks (Life Technology) and the electrophoresis buffer was
736 NuPAGE™ MOPS or MES SDS Running buffer (MOPS: Thermo Fisher NP0001; MES: Thermo
737 Fisher, NP0002) for 24-26 minutes at 220 volts. Proteins were transferred in a BioTrace™
738 nitrocellulose membrane (66485, Pall) in Mini PROTEAN Tetra System tanks (Bio Rad) for 90
739 minutes. at 100 volts. Membranes were blocked with 5% milk in Tween-TBS and then probed
740 with 1/1000 Anti-MYC (Santa Cruz, Biotechnology), 1/1000 anti-HA (Sigma, H3663) or 1/500
741 anti-yH2A (Abcam, ab15083). Primary antibodies were recognized by secondary antibodies
742 either anti-mouse or anti-rabbit IgG HRP-conjugated diluted 1/10000 (Thermo Fisher A11005

743 and A31556). Blots were developed using the ECL plus western blotting system (GE
744 Healthcare) during 10-30 sec.

745 qPCR

746 Cells were grown overnight in SC-Ade-His with 2% Raffinose at 30°C, diluted again in 2%
747 Raffinose until they reached the mid-log phase and then, 2% galactose was added to the
748 culture for I-*Sce*I induction. Cells were collected at 0, 2, 4 and 6 hours after galactose
749 induction. DNA was extracted from each sample using phenol/chloroform extraction. For this
750 purpose, cells were centrifuged 1 minute. at 13000 rpm, the pellet was mixed with 300 mg of
751 glass beads, 200 µL of lysis solution (Triton X-100 2 %, SDS 1 %, NaCl 100 mM, Tris 10 mM pH
752 8, EDTA 1 mM) and 200 µL phenol-chloroform-isoamyl alcohol (Sigma, 77617). The mix was
753 vortexed for 10 minutes at 4ºC and centrifuged for 10 minutes. at 13000 rpm at 4°C. 140 µL
754 of the supernatant was transferred into new tubes containing 500 µL ethanol 100% and DNA
755 was precipitated during 1 hour at 80ºC. The mix was centrifuged for 10 minutes. at 13000 rpm
756 at 4°C. The pellet was washed with 500 µL of ethanol 70 % and dried at room temperature
757 resuspended in 40 µL of TE containing 20 µg/µL of RNase (Roche, 10109169001) and
758 incubated 30 minutes. at 42°C. DNA concentrations were quantified using nanodrop.

759 qPCRs were prepared in a 360-wells plate. All samples were brought to a concentration of 5
760 ng/µL. In each well, 4µL of the sample were mixed with 4 µL of Power Track SYBR™ Green
761 master mix (Thermo Fisher A46109) and 0,3 µL of forward and reverses oligonucleotides (final
762 concentration 2.10^{-5} M). Oligonucleotides are listed in **Table 2**. I-*Sce*I oligonucleotides
763 generated a 187bp fragment that flanks the I-*Sce*I cutting site. ACT1 was used as a control to
764 normalize the samples. The standard curve was performed on actin (control) and I-*Sce*I cutting
765 site (before cut) to evaluate the efficiency of the couple of primers used. Triplicates from each
766 sample were performed and four 1:5 dilutions were performed for the standard curve.

767 Plate sampling was distributed by the epMotion 5070 robot (Eppendorf), qPCR was
768 performed with QuanStudio5 qPCR machine (Thermo Fisher) under the following conditions:
769 pre-incubation (95°C – 5 min – 4.4 °C/min), amplification (45 cycles; 95°C – 10 s - 4.4°C/min;
770 58°C – 10 s - 2.2 °C/min; 72°C – 20 s – 4,4 °C/min), melting curve (95°C – 5 s - 4.4 °C/min; 60°C
771 – 1 min – 2.2 °C/min; 97°C – continuous – 0.06 °C/min; 10 acquisitions/°C) and cooling (40°C

– 30 s - 2.2 °C/ min.). qPCR was analyzed with Thermo Fisher cloud and normalized by the Livak method ($2^{\Delta\Delta Ct}$) (Livak and Schmittgen, 2001).

Polymer model

The polymer model was identical to the one used in Liu et al. 2023 (Liu et al., 2023) which was based on the model of Arbona et al. 2017 (Arbona et al., 2017) but made in Polychrom (https://github.com/open2c/polychrom/tree/master), a python wrapper for polymer simulations using openMM (Eastman et al., 2017). The model consisted of a diploid yeast nucleus where each monomer represents 750 bp and is 15 nm in radius. The monomers were connected with harmonic bonds with a spring constant parameterized by a wiggle-distance w such that bond extensions of w lead to bond energies of 1kT

$$k = \frac{2k_B T}{w^2}.$$

From this follows that, in the absence of other forces, the wiggle distance will be equal to $\sqrt{2}$ times the bond standard deviation.

The beads were allowed to interact through the soft “polynomial_repulsive” potential. Stiffness was introduced through a harmonic force on the bond angle which favored alignment. The spring constant was chosen to yield a persistence length of 70 nm which was found optimal by Arbona et al. The nuclear envelope was modeled by a spherical confinement with a 1µm radius, and all telomeres were attached to the wall using strong harmonic bonds which allowed movement along the periphery but no radial motion. All centromeres were attached to the SPB using harmonic bonds with a 400 nm rest length and a high spring constant, allowing negligible fluctuations in length. The nucleolus was modeled by inserting 112,500 bp at the rDNA region where the size of monomers and bonds were increased by a factor 14. Long simulations were run to collect a set of starting configurations from which the starting conformation for short-time simulations were then randomly chosen upon initialization. The conversion factor between simulation time and experimental time was chosen to match the MSD of the 11kb loci in the WT condition.

Alphafold3 model

To predict potential interactions between the Smc5 hinge domain and candidate binding partners, the Smc5 hinge domain (residues 450–645) was modeled in complex with full-length (Tub1-Tub2), actin (Act1), or Shs1 subunit of the septin complex from *Saccharomyces cerevisiae*. Protein sequences were provided in FASTA format, and structural predictions were performed using default AlphaFold3 parameters. The confidence of the predicted interactions was evaluated using the interface predicted TM-score (iPTM), which reflects the likelihood of a specific protein-protein interaction.

Acknowledgements

We thank A. Marston, P. Hieter and T. Teixeira for sharing strains and plasmids. We also thank E. di Santo and C. Marquez for their participation in strains constructions. Our special thanks go to J. Reguera for his expertise on alpha-fold and his help on protein interaction modeling. Our acknowledgements go to S. Grosse-Holz, X. Zhao and J-M. Victor for enlightening discussions, P. Lesage, F. Garcia-Fernandez and S. Mihic for their constructive reading of the manuscript. P. Therizols and the members of the laboratory are thanked for the many lively discussions on this project and the GDR Architecture Dynamique du noyau et des génomes (ADN&G) for the valuable exchanges with its community. This work was supported by an FRM grant to EF (EQU202203014635) and CIHR grant to DD (FDN–167265). EF is also supported by PLBIO-INCA (PLBIO20-31) and DD by a Canada Research Chair in Chromatin Dynamics & Genome Architecture (CRC-2017-00064). ACS was supported by FRM (ECO202006011576) and ARC (ARCDOC42023010006078) fellowships.

References

Alt A, Dang HQ, Wells OS, Polo LM, Smith MA, McGregor GA, Welte T, Lehmann AR, Pearl LH, Murray JM, Oliver AW. 2017. Specialized interfaces of Smc5/6 control hinge stability and DNA association. *Nat Commun* **8**:14011. doi:10.1038/ncomms14011

Amitai A, Seeber A, Gasser SM, Holcman D. 2017. Visualization of Chromatin Decompaction and Break Site Extrusion as Predicted by Statistical Polymer Modeling of Single-Locus Trajectories. *Cell Rep* **18**:1200–1214. doi:10.1016/j.celrep.2017.01.018

Ampatzidou E, Irmisch A, O'Connell MJ, Murray JM. 2006. Smc5/6 Is Required for Repair at Collapsed Replication Forks. *Mol Cell Biol* **26**:9387–9401. doi:10.1128/MCB.01335-06

Aragón L. 2018. The Smc5/6 Complex: New and Old Functions of the Enigmatic Long-Distance Relative. *Annu Rev Genet* **52**:89–107. doi:10.1146/annurev-genet-120417-031353

Arbona JM, Herbert S, Fabre E, Zimmer C. 2017. Inferring the physical properties of yeast chromatin through Bayesian analysis of whole nucleus simulations. *Genome Biol* **18**. doi:10.1186/S13059-017-1199-X

Bermúdez-López M, Ceschia A, de Piccoli G, Colomina N, Pasero P, Aragón L, Torres-Rosell J. 2010. The Smc5/6 complex is required for dissolution of DNA-mediated sister chromatid linkages. *Nucleic Acids Res* **38**:6502. doi:10.1093/NAR/GKQ546

Biggins S. 2013. The Composition, Functions, and Regulation of the Budding Yeast Kinetochore. *Genetics* **194**:817. doi:10.1534/GENETICS.112.145276

Bloom K. 2024. Chromosome segregation: Brushing up on centromeres. *Current Biology* **34**:R565–R567. doi:10.1016/J.CUB.2024.04.074

Bouck DC, Bloom K. 2007. Pericentric Chromatin is an Elastic Component of the Mitotic Spindle. *Curr Biol* **17**:741. doi:10.1016/J.CUB.2007.03.033

Bouck DC, Bloom KS. 2005. The kinetochore protein Ndc10p is required for spindle stability and cytokinesis in yeast. *Proc Natl Acad Sci U S A* **102**:5408. doi:10.1073/PNAS.0405925102

Cabal GG, Genovesio A, Rodriguez-Navarro S, Zimmer C, Gadal O, Lesne A, Buc H, Feuerbach-Fournier F, Olivo-Marin JC, Hurt EC, Nehrbass U. 2006. SAGA interacting factors confine sub-diffusion of transcribed genes to the nuclear envelope. *Nature* **441**:770–773. doi:10.1038/NATURE04752

Caridi CP, D'agostino C, Ryu T, Zapotoczny G, Delabaere L, Li X, Khodaverdian VY, Amaral N, Lin E, Rau A, Chiolo I. 2018. Nuclear F-actin and myosins drive relocalization of heterochromatic breaks HHS Public Access. *Nature* **559**:54–60. doi:10.1038/s41586-018-0242-8

Cheblal A, Challa K, Seeber A, Shimada K, Yoshida H, Ferreira HC, Amitai A, Gasser SM. 2020. DNA Damage-Induced Nucleosome Depletion Enhances Homology Search Independently of Local Break Movement. *Mol Cell* **80**:311-326.e4. doi:10.1016/j.molcel.2020.09.002

Costantino L, Hsieh T-HSHS, Lamothe R, Darzacq X, Koshland D. 2020. Cohesin residency determines chromatin loop patterns. *Elife* **9**:1–31. doi:10.7554/eLife.59889

D'Ambrosio C, Schmidt CK, Katou Y, Kelly G, Itoh T, Shirahige K, Uhlmann F. 2008. Identification of cis-acting sites for condensin loading onto budding yeast chromosomes. *Genes Dev* **22**:2215. doi:10.1101/GAD.1675708

Dauban L, Montagne R, Thierry A, Lazar-Stefanita L, Bastié N, Gadal O, Cournac A, Koszul R, Beckouët F. 2020. Regulation of Cohesin-Mediated Chromosome Folding by Eco1 and Other Partners. *Mol Cell* **77**:1279-1293.e4. doi:10.1016/j.molcel.2020.01.019

Davidson IF, Bauer B, Goetz D, Tang W, Wutz G, Peters J-M. 2019. DNA loop extrusion by human cohesin. *Science (1979)* **366**:1338–1345. doi:10.1126/science.aaz3418

De Piccoli G, Cortes-Ledesma F, Ira G, Torres-Rosell J, Uhle S, Farmer S, Hwang JY, Machin F, Ceschia A, McAleenan A, Cordon-Preciado V, Clemente-Blanco A, Vilella-Mitjana F, Ullal P, Jarmuz A, Leitao B, Bressan D, Dotiwala F, Papusha A, Zhao X, Myung K, Haber JE, Aguilera A, Aragón L. 2006. Smc5-Smc6 mediate DNA double-strand-break repair by promoting sister-chromatid recombination. *Nat Cell Biol* **8**:1032–1034. doi:10.1038/ncb1466

Dion V, Kalck V, Seeber A, Schleker T, Gasser SM. 2013. Cohesin and the nucleolus constrain the mobility of spontaneous repair foci. *EMBO Rep* **14**:984–991. doi:10.1038/embor.2013.142

879 Eastman P, Swails J, Chodera JD, McGibbon RT, Zhao Y, Beauchamp KA, Wang LP,
880 Simmonett AC, Harrigan MP, Stern CD, Wiewiora RP, Brooks BR, Pande VS. 2017.
881 OpenMM 7: Rapid development of high performance algorithms for molecular
882 dynamics. *PLoS Comput Biol* **13**:e1005659. doi:10.1371/JOURNAL.PCBI.1005659
883 Fujioka Y, Kimata Y, Nomaguchi K, Watanabe K, Kohno K. 2002. Identification of a novel
884 non-structural maintenance of chromosomes (SMC) component of the SMC5-SMC6
885 complex involved in DNA repair. *Journal of Biological Chemistry* **277**:21585–21591.
886 doi:10.1074/jbc.M201523200
887 Gache V, Waridel P, Winter C, Juhem A, Schroeder M, Shevchenko A, Popov A V. 2010.
888 Xenopus Meiotic Microtubule-Associated Interactome. *PLoS One* **5**:9248.
889 doi:10.1371/JOURNAL.PONE.0009248
890 Ganji M, #2 IAS, Bisht S, Kim E, Kalichava A, Haering CH, Dekker C. 2018. Real-time
891 imaging of DNA loop extrusion by condensin. *Science (1979)* **360**:102–105.
892 doi:10.1126/science.aar7831
893 García Fernández F, Almayrac E, Carré Simon À, Batrin R, Khalil Y, Boissac M, Fabre E.
894 2022a. Global chromatin mobility induced by a DSB is dictated by chromosomal
895 conformation and defines the HR outcome. *Elife* **11**:1–25. doi:10.7554/eLife.78015
896 García Fernández F, Fabre E, Fernández FG, Fabre E, García Fernández F, Fabre E. 2022b.
897 The Dynamic Behavior of Chromatin in Response to DNA Double-Strand Breaks. *Genes*
898 *(Basel)* **13**:215. doi:10.3390/genes13020215
899 García Fernández F, Lemos B, Khalil Y, Batrin R, Haber JE, Fabre E. 2021. Modified
900 chromosome structure caused by phosphomimetic H2A modulates the DNA damage
901 response by increasing chromatin mobility in yeast. *J Cell Sci* **134**.
902 doi:10.1242/jcs.258500
903 Garcia-Luis J, Bordelet H, Thierry A, Koszul R, Aragon L. 2022. Depletion or cleavage of
904 cohesin during anaphase differentially affects chromatin structure and segregation. *Elife*
905 **11**. doi:10.7554/ELIFE.80147
906 Gutierrez-Escribano P, Hormeño S, Madariaga-Marcos J, Solé-Soler R, O'Reilly FJ, Morris
907 K, Aicart-Ramos C, Aramayo R, Montoya A, Kramer H, Rappsilber J, Torres-Rosell J,
908 Moreno-Herrero F, Aragon L, O'Reilly FJ, Morris K, Aicart-Ramos C, Aramayo R,
909 Montoya A, Kramer H, Rappsilber J, Torres-Rosell J, Moreno-Herrero F, Aragon L,
910 O'Reilly FJ, Morris K, Aicart-Ramos C, Aramayo R, Montoya A, Kramer H, Rappsilber
911 J, Torres-Rosell J, Moreno-Herrero F, Aragon L. 2020. Purified Smc5/6 Complex
912 Exhibits DNA Substrate Recognition and Compaction. *Mol Cell* **80**:1039-1054.e6.
913 doi:10.1016/j.molcel.2020.11.012
914 Hajjoul H, Mathon J, Ranchon H, Goiffon I, Mozziconacci J, Albert B, Carrivain P, Victor J-
915 MM, Gadal O, Bystricky K, Bancaud A. 2013. High-throughput chromatin motion
916 tracking in living yeast reveals the flexibility of the fiber throughout the genome.
917 *Genome Res* **23**:1829–1838. doi:10.1101/gr.157008.113
918 Harasymiw LA, Tank D, McClellan M, Panigrahy N, Gardner MK. 2019. Centromere
919 mechanical maturation during mammalian cell mitosis. *Nature Communications 2019*
920 *10:1* **10**:1–21. doi:10.1038/s41467-019-09578-z
921 Hauer MH, Gasser SM. 2017. Chromatin and nucleosome dynamics in DNA damage and
922 repair. *Genes Dev* **31**:2204–2221. doi:10.1101/gad.307702.117
923 Hauer MH, Seeber A, Singh V, Thierry R, Sack R, Amitai A, Kryzhanovska M, Eglinger J,
924 Holcman D, Owen-Hughes T, Gasser SM. 2017. Histone degradation in response to
925 DNA damage enhances chromatin dynamics and recombination rates. *Nat Struct Mol*
926 *Biol* **24**:99–107. doi:10.1038/nsmb.3347

He X, Asthana S, Sorger PK. 2000. Transient Sister Chromatid Separation and Elastic Deformation of Chromosomes during Mitosis in Budding Yeast. *Cell* **101**:763–775. doi:10.1016/S0092-8674(00)80888-0

Herbert S, Brion A, Arbona J, Lelek M, Veillet A, Lelandais B, Parmar J, Fernández FG, Almayrac E, Khalil Y, Birgy E, Fabre E, Zimmer C. 2017. Chromatin stiffening underlies enhanced locus mobility after DNA damage in budding yeast . *EMBO J* **36**:2595–2608. doi:10.15252/embj.201695842

Jeppsson K, Carlborg KK, Nakato R, Berta DG, Lilienthal I, Kanno T, Lindqvist A, Brink MC, Dantuma NP, Katou Y, Shirahige K, Sjögren C. 2014. The Chromosomal Association of the Smc5/6 Complex Depends on Cohesion and Predicts the Level of Sister Chromatid Entanglement. *PLoS Genet* **10**:e1004680. doi:10.1371/journal.pgen.1004680

Laflamme G, Tremblay-Boudreault T, Roy M-AA, Andersen P, Bonneil É, Atchia K, Thibault P, D'Amours D, Kwok BH. 2014. Structural maintenance of chromosome (SMC) proteins link microtubule stability to genome integrity. *Journal of Biological Chemistry* **289**:27418–27431. doi:10.1074/jbc.M114.569608

Lawrimore J, Barry TM, Barry RM, York AC, Friedman B, Cook DM, Akialis K, Tyler J, Vasquez P, Yeh E, Bloom K. 2017. Microtubule dynamics drive enhanced chromatin motion and mobilize telomeres in response to DNA damage. *Mol Biol Cell* **28**:1701–1711. doi:10.1091/mbc.E16-12-0846

Lawrimore J, Bloom K. 2022. Shaping centromeres to resist mitotic spindle forces. *J Cell Sci* **135**:jcs259532. doi:10.1242/jcs.259532

Lechner J, Carbon J. 1991. A 240 kd Multisubunit Protein Complex, CBF3, Is a Major Component of the Budding Yeast Centromere. *Cell* **64**:717–725.

Li Q, Zhang J, Haluska C, Zhang X, Wang Lei, Liu G, Wang Z, Jin D, Cheng T, Wang H, Tian Y, Wang X, Sun L, Zhao X, Chen Z, Wang Lanfeng. 2024. Cryo-EM structures of Smc5/6 in multiple states reveal its assembly and functional mechanisms. *Nature Structural & Molecular Biology 2024 31:10* **31**:1532–1542. doi:10.1038/S41594-024-01319-1

Lindroos HB, Ström L, Itoh T, Katou Y, Shirahige K, Sjögren C, Betts Lindroos H, Ström L, Itoh T, Katou Y, Shirahige K, Sjögren C, Lindroos HB, Ström L, Itoh T, Katou Y, Shirahige K, Sjögren C, Betts Lindroos H, Ström L, Itoh T, Katou Y, Shirahige K, Sjögren C. 2006. Chromosomal Association of the Smc5/6 Complex Reveals that It Functions in Differently Regulated Pathways. *Mol Cell* **22**:755–767. doi:10.1016/j.molcel.2006.05.014

Lisby M, Rothstein R, Mortensen UH. 2001. Rad52 forms DNA repair and recombination centers during S phase. *Proceedings of the National Academy of Sciences* **98**:8276–8282. doi:10.1073/pnas.121006298

Liu S, Miné-Hattab J, Villemeur M, Guerois R, Pinholt HD, Mirny LA, Taddei A. 2023. In vivo tracking of functionally tagged Rad51 unveils a robust strategy of homology search. *Nat Struct Mol Biol* **30**:1582–1591. doi:10.1038/s41594-023-01065-w

Livak KJ, Schmittgen TD. 2001. Analysis of Relative Gene Expression Data Using Real-Time Quantitative PCR and the 2−ΔΔCT Method. *Methods* **25**:402–408. doi:10.1006/METH.2001.1262

Marshall WF, Straight A, Marko JF, Swedlow J, Dernburg A, Belmont A, Murray AW, Agard DA, Sedat JW. 1997. Interphase chromosomes undergo constrained diffusional motion in living cells. *Current Biology* **7**:930–939. doi:10.1016/S0960-9822(06)00412-X

Maskell DP, Hu XW, Singleton MR. 2010. Molecular architecture and assembly of the yeast kinetochore MIND complex. *J Cell Biol* **190**:823. doi:10.1083/JCB.201002059

976 Megee PC, Mistrot C, Guacci V, Koshland D. 1999. The centromeric sister chromatid
977 cohesion site directs Mcd1p binding to adjacent sequences. *Mol Cell* **4**:445–450.
978 doi:10.1016/S1097-2765(00)80347-0
979 Mendoza M, Norden C, Durrer K, Rauter H, Uhlmann F, Barral Y. 2009. A mechanism for
980 chromosome segregation sensing by the NoCut checkpoint. *Nat Cell Biol* **11**:477–483.
981 doi:10.1038/NCB1855
982 Miné-Hattab J, Recamier V, Izeddin I, Rothstein R, Darzacq X. 2017. Multi-scale tracking
983 reveals scale-dependent chromatin dynamics after DNA damage. *Mol Biol Cell* **28**:3323–
984 3332. doi:10.1091/mbc.E17-05-0317
985 Miné-Hattab J, Rothstein R. 2012. Increased chromosome mobility facilitates homology
986 search during recombination. *Nat Cell Biol* **14**:510–517. doi:10.1038/ncb2472
987 Misteli T. 2020. The Self-Organizing Genome: Principles of Genome Architecture and
988 Function. *Cell* **183**:28–45. doi:10.1016/j.cell.2020.09.014
989 Mora-Bermúdez F, Gerlich D, Ellenberg J. 2007. Maximal chromosome compaction occurs
990 by axial shortening in anaphase and depends on Aurora kinase. *Nat Cell Biol* **9**:822–831.
991 doi:10.1038/NCB1606,
992 Moradi-Fard S, Sarthi J, Tittel-Elmer M, Lalonde M, Cusanelli E, Chartrand P, Cobb JA.
993 2016. Smc5/6 Is a Telomere-Associated Complex that Regulates Sir4 Binding and TPE.
994 *PLoS Genet* **12**. doi:10.1371/journal.pgen.1006268
995 Morawska M, Ulrich HD. 2013. An expanded tool kit for the auxin-inducible degron system
996 in budding yeast. *Yeast* **30**:341–351. doi:https://doi.org/10.1002/yea.2967
997 Neumann FR, Dion V, Gehlen LR, Tsai-Pflugfelder M, Schmid R, Taddei A, Gasser SM.
998 2012. Targeted INO80 enhances subnuclear chromatin movement and ectopic
999 homologous recombination. *Genes Dev* **26**:369–383. doi:10.1101/gad.176156.111
1000 Nishimura K, Kanemaki MT. 2014. Rapid Depletion of Budding Yeast Proteins via the
1001 Fusion of an Auxin-Inducible Degron (AID). *Curr Protoc Cell Biol* **64**:20.9.1-20.9.16.
1002 doi:10.1002/0471143030.CB2009S64
1003 Norden C, Mendoza M, Dobbelaere J, Kotwaliwale C V, Biggins S, Barral Y. 2006. The
1004 NoCut Pathway Links Completion of Cytokinesis to Spindle Midzone Function to
1005 Prevent Chromosome Breakage. *Cell* **125**:85–98. doi:10.1016/j.cell.2006.01.045
1006 Oshidari R, Strecker J, Chung DKCC, Abraham KJ, Chan JNYY, Damaren CJ, Mekhail K.
1007 2018. Nuclear microtubule filaments mediate non-linear directional motion of chromatin
1008 and promote DNA repair. *Nat Commun* **9**. doi:10.1038/s41467-018-05009-7
1009 Paldi F, Alver B, Robertson D, Schalbetter SA, Kerr A, Kelly DA, Baxter J, Neale MJ,
1010 Marston AL. 2020. Convergent genes shape budding yeast pericentromeres. *Nature 2020*
1011 *582:7810* **582**:119–123. doi:10.1038/S41586-020-2244-6
1012 Panja D, Barkema GT. 2009. Rouse modes of self-avoiding flexible polymers. *Journal of*
1013 *Chemical Physics* **131**. doi:10.1063/1.3244678/316841
1014 Pebernard S, Wohlschlegel J, Mcdonald WH, Yates Iii JR, Boddy MN. 2006. The Nse5-Nse6
1015 Dimer Mediates DNA Repair Roles of the Smc5-Smc6 Complex. *Mol Cell Biol*
1016 **26**:1617–1630. doi:10.1128/MCB.26.5.1617-1630.2006
1017 Pellicioli A, Lucca C, Liberi G, Marini F, Lopes M, Plevani P, Romano A, Di Fiore PP,
1018 Foiani M. 1999. Activation of Rad53 kinase in response to DNA damage and its effect in
1019 modulating phosphorylation of the lagging strand DNA polymerase. *EMBO J* **18**:6561–
1020 6572. doi:10.1093/EMBOJ/18.22.6561
1021 Peng XP, Lim S, Li S, Marjavaara L, Chabes A, Zhao X. 2018. Acute Smc5/6 depletion
1022 reveals its primary role in rDNA replication by restraining recombination at fork pausing
1023 sites. *PLoS Genet* **14**. doi:10.1371/journal.pgen.1007129

1024 Phipps J, Toulouze M, Ducrot C, Costa R, Brocas C, Dubrana K. 2024. Cohesin complex
1025 oligomerization maintains end-tethering at DNA double-strand breaks. *Nature Cell*
1026 *Biology 2024 27:1* **27**:118–129. doi:10.1038/s41556-024-01552-2
1027 Potts PR, Porteus MH, Yu H. 2006. Human SMC5/6 complex promotes sister chromatid
1028 homologous recombination by recruiting the SMC1/3 cohesin complex to double-strand
1029 breaks. *EMBO J* **25**:3377–3388. doi:10.1038/sj.emboj.7601218
1030 Pradhan B, Kanno T, Umeda Igarashi M, Loke MS, Baaske MD, Wong JSK, Jeppsson K,
1031 Björkegren C, Kim E. 2023. The Smc5/6 complex is a DNA loop-extruding motor.
1032 *Nature 2023 616:7958* **616**:843–848. doi:10.1038/s41586-023-05963-3
1033 Ratsima H, Ladouceur AM, Pascariu M, Sauvé V, Salloum Z, Maddox PS, D'Amours D.
1034 2011. Independent modulation of the kinase and polo-box activities of Cdc5 protein
1035 unravels unique roles in the maintenance of genome stability. *Proc Natl Acad Sci U S A*
1036 **108**. doi:10.1073/PNAS.1106448108
1037 Richmond D, Rizkallah R, Liang F, Hurt MM, Wang Y. 2013. A Highlights from MBoC
1038 Selection: Slk19 clusters kinetochores and facilitates chromosome bipolar attachment.
1039 *Mol Biol Cell* **24**:566. doi:10.1091/MBC.E12-07-0552
1040 Roy M-AA, Siddiqui N, D'Amours D. 2011. Dynamic and selective DNA-binding activity of
1041 Smc5, a core component of the Smc5-Smc6 complex. *Cell Cycle* **10**:690–700.
1042 doi:10.4161/cc.10.4.14860
1043 Roy S, Adhikary H, D'Amours D. 2024. The SMC5 / 6 complex: folding chromosomes back
1044 into shape when genomes take a break. *Nucleic Acids Res* **52**:2112–2129.
1045 doi:10.1093/nar/gkae103
1046 Ryu T, Spatola B, Delabaere L, Bowlin K, Hopp H, Kunitake R, Karpen GH, Chiolo I. 2015.
1047 Heterochromatic breaks move to the nuclear periphery to continue recombinational
1048 repair. *Nat Cell Biol* **17**:1401. doi:10.1038/NCB3258
1049 Serrano D, Cordero G, Kawamura R, Sverzhinsky A, Sarker M, Roy S, Malo C, Pascal JM,
1050 Marko JF, D'Amours D. 2020. The Smc5/6 Core Complex Is a Structure-Specific DNA
1051 Binding and Compacting Machine. *Mol Cell* **80**:1025-1038.e5.
1052 doi:10.1016/j.molcel.2020.11.011
1053 Shroff R, Arbel-Eden A, Pilch D, Ira G, Bonner WM, Petrini JH, Haber JE, Lichten M. 2004.
1054 Distribution and Dynamics of Chromatin Modification Induced by a Defined DNA
1055 Double-Strand Break. *Current Biology* **14**:1703–1711. doi:10.1016/j.cub.2004.09.047
1056 Socol M, Wang R, Jost D, Carrivain P, Vaillant C, Le Cam E, Dahirel V, Normand C,
1057 Bystricky K, Victor JM, Gadal O, Bancaud A. 2019. Rouse model with transient
1058 intramolecular contacts on a timescale of seconds recapitulates folding and fluctuation of
1059 yeast chromosomes. *Nucleic Acids Res* **47**:6195–6207. doi:10.1093/NAR/GKZ374
1060 Stephens AD, Haase J, Vicci L, Taylor RM, Bloom K. 2011. Cohesin, condensin, and the
1061 intramolecular centromere loop together generate the mitotic chromatin spring. *J Cell*
1062 *Biol* **193**:1167. doi:10.1083/JCB.201103138
1063 Strecker J, Gupta GD, Zhang W, Bashkurov M, Landry M-CC, Pelletier L, Durocher D.
1064 2016. DNA damage signalling targets the kinetochore to promote chromatin mobility.
1065 *Nat Cell Biol* **18**:281–290. doi:10.1038/ncb3308
1066 Symington LS, Gautier J. 2011. Double-strand break end resection and repair pathway
1067 choice. *Annu Rev Genet* **45**:247–271. doi:10.1146/ANNUREV-GENET-110410-
1068 132435/CITE/REFWORKS
1069 Talbert PB, Henikoff S. 2020. What makes a centromere? *Exp Cell Res* **389**:111895.
1070 doi:10.1016/J.YEXCR.2020.111895
1071 Tanaka T, Cosma MP, Wirth K, Nasmyth K. 1999. Identification of cohesin association sites
1072 at centromeres and along chromosome arms. *Cell* **98**:847–858. doi:10.1016/S0092-
1073 8674(00)81518-4

1074 Therizols P, Duong T, Dujon B, Zimmer C, Fabre E, Therizolsa P, Duong T, Dujon B,
1075 Zimmer C, Fabre E, Therizols P, Duong T, Dujon B, Zimmer C, Fabre E. 2010.
1076 Chromosome arm length and nuclear constraints determine the dynamic relationship of
1077 yeast subtelomeres. *Proc Natl Acad Sci U S A* **107**:2025–2030.
1078 doi:10.1073/pnas.0914187107
1079 Torres-Rosell J, Machín F, Farmer S, Jarmuz A, Eydmann T, Dalgaard JZ, Aragón L, Mahín
1080 F, Farmer S, Jarmuz A, Eydmann T, Dalgaard JZ, Aragón L, Machín F, Farmer S,
1081 Jarmuz A, Eydmann T, Dalgaard JZ, Aragón L. 2005. SMC5 and SMC6 genes are
1082 required for the segregation of repetitive chromosome regions. *Nat Cell Biol* **7**:412–419.
1083 doi:10.1038/ncb1239
1084 Torres-Rosell J, Sunjevaric I, De Piccoli G, Sacher M, Eckert-Boulet N, Reid R, Jentsch S,
1085 Rothstein R, Aragón L, Lisby M. 2007. The Smc5-Smc6 complex and SUMO
1086 modification of Rad52 regulates recombinational repair at the ribosomal gene locus. *Nat*
1087 *Cell Biol* **9**:923–931. doi:10.1038/ncb1619
1088 Venegas AB, Natsume T, Kanemaki M, Hickson ID. 2020. Inducible Degradation of the
1089 Human SMC5/6 Complex Reveals an Essential Role Only during Interphase. *Cell Rep*
1090 **31**:107533. doi:10.1016/j.celrep.2020.107533
1091 Verdaasdonk JS, Gardner R, Stephens AD, Yeh E, Bloom K. 2012. Tension-dependent
1092 nucleosome remodeling at the pericentromere in yeast. *Mol Biol Cell* **23**:2560–2570.
1093 doi:10.1091/mbc.E11-07-0651
1094 Verdaasdonk JS, Vasquez PA, Barry RM, Barry T, Goodwin S, Forest MG, Bloom K. 2013.
1095 Centromere tethering confines chromosome domains. *Mol Cell*
1096 **52**:10.1016/j.molcel.2013.10.021. doi:10.1016/j.molcel.2013.10.021
1097 Wang ZA, Cole PA. 2020. The Chemical Biology of Reversible Lysine Post-Translational
1098 Modifications. *Cell Chem Biol* **27**:953. doi:10.1016/J.CHEMBIOL.2020.07.002
1099 Wigge PA, Kilmartin J V. 2001. The Ndc80p complex from Saccharomyces cerevisiae
1100 contains conserved centromere components and has a function in chromosome
1101 segregation. *J Cell Biol* **152**:349–360. doi:10.1083/JCB.152.2.349
1102 Zhao X, Blobel G. 2005. A SUMO ligase is part of a nuclear multiprotein complex that
1103 affects DNA repair and chromosomal organization. *Proc Natl Acad Sci U S A* **102**:4777.
1104 doi:10.1073/PNAS.0500537102
1105

1106 ## Figures

1107 **Figure 1: The *smc5-2KE* mutant shows decreased binding affinity to microtubules *in vitro***
1108 **and leads to an increased chromatin dynamics at pericentromeres and beyond. (A)**
1109 Representation of the CryoEM of the Smc5-Smc6 hinge from Li et al., NSMB, 2024 (PDB:
1110 7YLM). The Smc5 hinge domain is shown in blue, the Smc6 hinge in green, and Nse2 in brown.
1111 Lysines 624, 631, and 667 are highlighted in purple. **(B)** AlphaFold model of the Smc5 hinge
1112 (amino acids 450–645) showing a high predicted probability of interaction with tubulin
1113 dimers. Lysines 631 and 624 (in purple) contact adjacent tubulin subunits in the microtubule.
1114 Smc5 is shown as a cartoon in light blue; tubulin dimers are colored individually. **(C)** The
1115 fraction of microtubule-bound Smc5 and Smc5-2KE from 3 independent experiments was
1116 plotted as a function of microtubules (MT) concentrations. Dissociation constants (Kd) were

1117 determined by curve fitting to a hyperbola. **(D)** Co-immunoprecipitation (co-IP) experiments
1118 showing the association of Nse3-3xSTII with Smc5 or Smc5-2KE proteins (both tagged with C-
1119 terminal 13xMYC epitopes) in yeast extracts. A whole cell extract was loaded as an input (7%;
1120 **left**) and Smc5/6 complex components were immunoprecipitated from this extract using
1121 StrepTactin XT® resin (**right**). For each panel, the first lane represents a negative control
1122 where only Nse3 was tagged (with 3xSTII), whereas the second and third lanes show Nse3-
1123 3xSTII co-purified with Smc5-13xMYC and Smc5-2KE-13xMYC proteins, respectively. **(E)** Mean
1124 square displacement (MSDs) as a function of increasing time intervals in the WT (blue) and in
1125 the *smc5*-2KE mutant (green) for a locus at different positions of chromosome IV (11kb, 90 kb
1126 and 730 kb, from left to right). Wilcoxon rank-sum test results between distributions, with the
1127 p-value. * ($p<0.05$), *** ($p<0.0001$). **(F)** Distributions of the exponent alpha (upper line) and
1128 of the sub-diffusion coefficient D (lower line) for the WT (blue) and in the *smc5-2KE* mutant
1129 (green) for loci at different positions of chromosome IV. The values of parameters alpha and
1130 D are calculated from single trajectories as described in Material and Methods. Vertical lines
1131 correspond to average values (WT in blue, *smc5-2KE* mutant in green).

1132 **Figure 2: The binding of microtubules to kinetochore is necessary but not sufficient to**
1133 **control pericentromeric chromatin dynamics. (A)** Experimental protocol used to
1134 depolymerize microtubules with 15 ng/µl of nocodazole while continued cycling. **(B)** Tub2-
1135 GFP in the WT and in the *smc5-2KE* mutant with or without addition of nocodazole. **(C)** Cells
1136 synchronization monitored by flow cytometry in cells treated with nocodazole (15 ng/µl).
1137 Samples were taken at 0, 30 and 120 minutes after nocodazole addition. **(D)** MSD as a function
1138 of increasing time intervals in the WT and *smc5*-2KE mutant at 11, 90 and 730 kb with or
1139 without the presence of nocodazole. Wilcoxon rank-sum test results between distributions,
1140 with the p-value "ns" non-significant, *** ($p<0.0001$). **(E)** MSDs as a function of increasing
1141 time intervals of the locus at 90 kb in the *ndc80-1* mutant (**left**) and *ndc10-1* mutant (**right**)
1142 combined with or without the Smc5-2KE mutation at 37°C. Wilcoxon rank-sum test results
1143 between distributions, with the p-value "ns" non-significant, *** ($p<0.0001$) **(F)** Table
1144 summarizing the different conditions with values extracted from the MSD: MSD at 10 s, the
1145 anomalous exponent (alpha), the sub-diffusive coefficient (D) and the number of cells
1146 analyzed.

1147 **Figure 3: The *smc5-2KE* mutant changes chromatin properties in the pericentromeric region.**
1148 **(A-B)** Cumulative distribution functions (CDF) show the intrachromosomal distances
1149 distribution measured for two pairs of loci 180 kb apart at two different positions of the
1150 chromosome IV, **(A)** close to the centromere (R1) and **(B)** in the middle of the arm (R3) in the
1151 presence or absence of Zeocin. Three experiments were done in each case: R1: N_{WT}=21806,
1152 N_{2KE}=9014, $N_{WT\ ZEO}$=4091, $N_{2KE\ ZEO}$=1570 and for R3: N_{WT}=2778, N_{2KE}=4403. Wilcoxon rank-sum
1153 test was used to analyze with *** for P<0.001.

1154 **Figure 4: Polymer model recapitulates changes in chromatin dynamics at pericentromeres.**
1155 **(A)** Comparison of MSDs for loci with various distances to the centromere. **(B)** Effect of
1156 increasing the flexibility of the SPB tether from rigid (red curves) to a spring constant of 1kbT/
1157 $(105\ nm)^2$ which would allow for a standard deviation of 74 nm (105 nm/sqrt(2)) if no other
1158 forces were applied (blue curves). Left plot shows loci 11kb from the centromere and the right
1159 shows loci 90 kb from the centromere. Only loci on chromosomes larger than 400 kb excluding
1160 Chr XII were included. The inset shows a 2D slice of the centromere positions for the loose
1161 (blue) and rigid (red) centromeres. Bonds are shown in grey and scale bar is 500 nm. **(C)** Effect
1162 of increasing polymer stiffness from one leading to a persistence length of 70 nm (red curves)
1163 to one with an angular spring constant that is 20% higher (blue curves). Loci are as in (B). Inset
1164 shows a 2D conformation of Chr I in the two conditions, scale bar is 500 nm. **(D)** MSD for loci
1165 11 kb away from the centromere when comparing effects of increasing flexibility (blue and
1166 red curves, same as left panel of (B)) and combining flexibility and stiffness (grey curve).

1167 **Figure 5: The *smc5-2KE* mutant alters the mitotic spindle integrity. (A)** CEN IV was tagged
1168 with GFP and SPB with Spc42-mCherry. 2D distances between two SPBs (red dots) (**left**) and
1169 between Cen (green) and SPB (red) in G2/M cells (**right**) were measured in three independent
1170 biological replicates., Number of cells for SPB-SPB (N_{WT}=224, N_{2KE}=332) and for CEN-SPB
1171 (N_{WT}=247, N_{2KE}=380). As a positive control, CEN-SPB was measured in the presence of Zeocin
1172 with $N_{WT\ ZEO}$=1299, $N_{2KE\ ZEO}$=2033. Wilcoxon rank-sum test was used to analyze differences
1173 between groups, with "ns" for not significant and *** for P<0.0001. **(B)** Examples of cycling
1174 and defective mitotic cells are shown (top) and cycle phase distribution quantification
1175 (bottom) in *Mtw1-3xGFP* (WT) and *Smc5-2KE Mtw1-3xGFP* (2KE) cells, in the presence or not
1176 of deletion of *Mad2 (Δmad2)* or *Bub1* (*Δbub1*). Cells were categorized into G1, S, or G2/M

1177 phases. Additionally, dead cells and those exhibiting no-cut phenotype (no-cut) were counted
1178 in three experimental replicates N number of cells were counted N_{WT}=439, $N_{WT\ NOC}$=588,
1179 N_{2KE}=413, $N_{2KE\ NOC}$=652. T-test was used to analyze with * for P<0.01 and ** for P<0.001. **(C)**
1180 Mtw1 was labelled with 3xGFP to measure kinetochore clusters with or without nocodazole
1181 addition (15 ng/µl). Percentage of non-clustered cells are plotted. T- test was used to analyze
1182 differences between groups, with "ns" for not significant, ** for (P<0.001).

1183 **Figure 6: The *smc5-2KE* mutant decreases homologous recombination efficiency at**
1184 **pericentromeres. (A)** Schematic representation of the system to track homologous
1185 recombination (HR). In the recipient mCherry, I-*Sce*I has a 30 bp I-*Sce*I cutting site sequence
1186 followed by a stop codon (red bar) inserted at 57 amino acids from the end of
1187 the mCherry coding sequence. The donor (dCen) is a full-length mCherry lacking promoter
1188 and terminator sequences, carried on a centromeric plasmid. A functional mCherry could be
1189 expressed only after successful HR. **(B)** Colony formation unit (CFU) test showing three
1190 conditions: without DSB (-DSB), with a DSB (+DSB) and with a DSB and a donor (DSB+donor)
1191 in the C and in the L strain for the WT and for the *smc5-2KE* mutant. Ratio between Induced
1192 I-*Sce*I/Non induced I-*Sce*I. Three experiments were conducted with the number of cells
1193 counted as follows: For the C strain, $N_{WT\ PRS}$ =487, $N_{WT\ PB}$ =528, $N_{WT\ Cen}$ =668, $N_{2KE\ PRS}$ =330, N_{2KE}
1194 $_{PB}$ =620, $N_{2KE\ Cen}$ =752. For the L strain, $N_{WT\ PRS}$ =344, $N_{WT\ PB}$ =309, $N_{WT\ Cen}$ =328, $N_{2KE\ PRS}$ = 261,
1195 $N_{2KE\ PB}$ =379, $N_{2KE\ Cen}$ =387. Mann-Whitney test was used to analyse differences between
1196 groups, with "ns" for not significant (P>0.05) and ** for P<0.001. **(C)** Number of red cells (%)
1197 without DSB (-DSB), with a DSB (+DSB) and with a DSB and a donor (DSB+donor) in the C and
1198 in the L strain. Three experiments were conducted, counting the number of cells for the C
1199 strain as follows: $N_{WT\ PRS}$ =707, $N_{WT\ PB}$ =719, $N_{WT\ Cen}$ =2180, $N_{2KE\ PRS}$ = 727, $N_{2KE\ PB}$ =660, $N_{2KE\ Cen}$
1200 =2553. For the L strain, the counts were $N_{WT\ PRS}$ =506, $N_{WT\ PB}$ =607, $N_{WT\ Cen}$ =1299, $N_{2KE\ PRS}$ =744,
1201 $N_{2KE\ PB}$ =712, $N_{2KE\ Cen}$ =1551. Mann-Whitney test was used to analyse differences between
1202 groups, with "ns" for not significant (P>0.05) and * for P<0.005.

1203 Supplemental material

1204 **Figure supplement 1: Mass spectrometry analysis of proteins co-purifying with the yeast**
1205 **Smc5/6 complex.** The Smc5/6 complex was isolated from crude extracts using Ni-NTA and
1206 Strep-Tactin affinity chromatography and purified proteins were subjected to mass

1207 spectrometry analysis. **(A)** Silver-stained gel showing the 8 subunits of the yeast Smc5/6
1208 complex obtained after consecutive rounds of Ni-NTA and Strep-Tactin affinity
1209 chromatography. The expected positions of Smc5/6 subunits are marked next to the gel. **(B)**
1210 Amino acid sequence of the beta chain of yeast tubulin (Tub2). High probability peptide
1211 sequences identified in the mass spectrometry analysis are highlighted in yellow. **(C)** Tub2
1212 peptides detected by mass spectrometry and their probability of identification.
1213
1214 **Figure supplement 2: Smc5-2KE mutation does not affect cell growth nor cell cycle. (A)** Table
1215 showing AlphaFold3 predictions of interactions between the Smc5 hinge domain (residues
1216 450–645) and candidate proteins. Only the Tub1/Tub2 complex showed a high-confidence
1217 interaction (ipTM = 0.72), while Shs1 displayed low ipTM scores, indicating weak or no
1218 predicted interaction**. (B)** Microtubule polymer binding assay. Coomassie blue-stained gels
1219 showing the binding of the hinge region of Smc5 (residues 215–885) to the microtubule (MT,
1220 µM) polymer fraction (pellet; P) after centrifugation. Note how Smc5 hinge domain
1221 progressively transferred from the depolymerized tubulin fraction (supernatant; S) to the
1222 polymer fraction (P) as the MT concentration increased and eventually bound all available
1223 Smc5 protein (top gel). In contrast, the Smc5-2KE mutant (lower gel) showed strongly reduced
1224 affinity for MT polymers, as evidenced by the substantial fraction of the hinge domain
1225 remaining in the supernatant fraction at the highest concentration of MT shown in the gel (4
1226 µM). **(C)** Experimental protocol used to synchronize cells in G1 using alpha factor. **(D)**
1227 Percentage of budded and late anaphase cells at each time point, respectively. **(E)** Cell
1228 synchronization monitored by flow cytometry. **(F)** Images showing examples of G1 (**left**),
1229 metaphase (**middle**) and anaphase (**right**) cell morphologies monitored in yeast cultures
1230 expressing Smc5 o*r* smc5-2KE. Prior to imaging, cells were fixed, washed and stained with
1231 DAPI to enable nuclei visualization. Scale bars represent 5µm. **(G-H)** Growth phenotypes on
1232 solid medium **(G)** in the presence of DNA-damaging agents — 100 mM hydroxyurea (HU), 10
1233 µM camptothecin (CPT), or 4-nitroquinoline-1-oxide (4NQO) and **(H)** at different
1234 temperatures. 1/10 serial dilutions were spotted and photographed after 48h **(I)**
1235 Chromosomal association of Smc5-MYC at selected loci in the indicated strains, as determined
1236 by ChIP-qPCR. Cells were arrested in G2/M prior to sample collection. The Y-axis represents
1237 the amount of DNA in the ChIP fraction relative to input. Primers were designed to amplify
1238 the centromeres of chromosomes 9 (Cen9) and 13 (Cen13), the *rDNA* non-transcribed spacer

1239 1 (Nts1), telomere 15 (Tel15). *ACT1* gene is used as a control. Each bar shows the mean of
1240 three independent experiments, with standard deviations indicated. Statistical significance
1241 was assessed using a two-tailed Student's t-test. P-values are denoted as follows: n.s. = not
1242 significant (p > 0.05).

1243 **Figure supplement 3: The negative charges of K624E and K631E, and not post-translational**
1244 **modifications, lead to increased chromatin mobility along the chromosomal arm in smc5-**
1245 **2KE with no effect on chromatin cohesion. (A)** Table summarizing the different conditions
1246 with values extracted from the MSD: MSD at 10 s, the anomalous exponent (alpha), the sub-
1247 diffusive coefficient (D) and the number of cells analyzed. **(B)** MSDs as a function of increasing
1248 time intervals on a log-log scale in the WT (blue) and in the *smc5*-2KE mutant (green) for a
1249 locus at different positions of chromosome IV (11kb, 90 kb and 730 kb, from left to right).
1250 Wilcoxon rank-sum test results between distributions, with the p-value. * (p<0.05), ***
1251 (p<0.0001). **(C)** Ratio of MSD at 10 s between *smc5-2KE* versus WT at different positions of
1252 the chromosome IV. **(D)** MSDs as function of time in the WT, *smc5-2KR* and *smc5-2KE*
1253 mutants. Wilcoxon rank-sum test results between distributions, with the p-value. ns (p>0.05)
1254 and *** (p<0.0001). **(E-F)** Cohesion status was assessed based on the number of GFP foci
1255 separation of tetO/TetR-GFP marker at ~11 kb from the centromere of chromosome IV in
1256 metaphase. Cells were synchronized by Cdc20 depletion. **(E)** WT Smc5 or the *smc5-2KE*
1257 mutated cells, and **(F)** cells in which Smc1 was tagged with an auxin-inducible degron. Cells
1258 with a single GFP (yellow) dot were scored as having cohesive sister chromatids, while cells
1259 with two GFP foci (purple) were scored as having defective cohesion. For each biological
1260 replicate, 200 cells were scored. Data show means of three replicates, with error bars
1261 representing ± sd; unpaired two-tailed t-test was used to analyze differences between groups,
1262 with "ns" for not significant (P>0.05) and * for P<0.01.

1263 **Figure supplement 4. Smc5-2KE mutation increases chromatin mobility throughout the cell**
1264 **cycle. (A)** Experimental protocol used to synchronize cells in G1 with 50 ng/ml of alpha factor
1265 (**left**). WT and *smc5*-2KE MSDs at 11 and 90 Kb at G1. Wilcoxon rank-sum test results between
1266 distributions, with the p-value *** (p<0.0001) (**right**). **(B)** Experimental protocol used to
1267 synchronize in G2/M cells carrying the P_{MET3}-*CDC20* with 2 mM of methionine (**left**). WT and
1268 *smc5-2KE* MSDs at 11 and 23 Kb at G2/M phase. Wilcoxon rank-sum test results between

1269 distributions, with the p-value *** (p<0.0001) (**right**). **(C)** Table summarizing the different
1270 conditions with values extracted from the MSD: MSD at 10 sec, the alpha, the sub-diffusive
1271 coefficient (D) and the number of cells analyzed.

1272 **Figure supplement 5. The *smc5-2KE* mutant does not induce spontaneous DNA damage. (A)**
1273 Rad52-foci (protein involved in HR) in WT and *smc5-2KE* mutant (2KE). Three independent
1274 experiments were conducted with the number of cells counted as follows: N_{WT}=608,
1275 N_{2KE}=1388, $N_{WT\ ZEO}$=650, $N_{2KE\ ZEO}$=509. T-test was used to analyze differences between groups,
1276 with "ns" for not significant and *** for P<0.0001. **(B)** Representative results from
1277 immunoblotting showing the phosphorylation (Ph) status of Rad53 in WT, *smc5-2KE* cells and
1278 in response to Zeocin treatment (zeo). Actin was used as a loading control. Blots are
1279 representative of three experiments. **(C)** Representative results from immunoblotting
1280 showing the phosphorylation of H2A (γH2A) in WT, *smc5-2KE* cells and in response to Zeocin
1281 treatment. Actin was used as a loading control. Blots are representative of three experiments
1282 (**left**). Protein levels are represented as mean ratio values quantified from protein γH2A
1283 versus actin (**right**).

1284 **Figure supplement 6. The Smc5 or Smc6 degradation decreases chromatin dynamics. (A)**
1285 Experimental protocol used to synchronize cells in metaphase with 2 mM of methionine cells
1286 carrying the P_{MET3}-*CDC20*, followed by degradation of SMCs with 1mM auxin for 1 hour prior
1287 to imaging. Auxin being diluted in ethanol (EtOH), controls with EtOH only were performed
1288 **(B)** Growth phenotypes on solid medium with or without Auxin in WT, Smc5-AID, Smc6-AID
1289 and Smc1-AID **(C)** Representative results from immunoblotting showing the degradation of
1290 the Smc5 upon 30 minutes of treatment with 1 mM auxin. Actin was used as a loading control.
1291 Blots are representative of three experiments. **(D-E)** MSDs as a function of increasing time
1292 intervals in the absence of auxin (dark blue) and in the presence of Auxin (light blue) in a locus
1293 at 11kb from the CEN4 in **(D)** Smc5-AID, Smc6-AID and **(E)** Smc1-AID. Wilcoxon rank-sum test
1294 results between distributions, with the p-value *** (p<0.0001). **(F)** Table summarizing the
1295 different conditions with values extracted from the MSD: MSD at 10 sec, the anomalous
1296 exponent (alpha), the sub-diffusive coefficient (D) and the number of cells analyzed.

1297 **Figure supplement 7. Weakening the microtubule tether to the kinetochore gradually**
1298 **abolishes position-dependent mobility:** Sweep of the wiggle distance (wd) of the bond

1299 connecting the centromere to the spindle pole body (See material and methods for a
1300 mathematical definition of wd. In the absence of other forces it is $\sqrt{2}$ times the bond standard
1301 deviation). **(A)** MSD of loci 11 kb from the centromere. **(B)** MSD of loci 90 kb from the
1302 centromere. Candidate loci are selected as in Figure 4 and wild type (WT) refers to the
1303 simulation in Figure 4A.

1304 **Figure supplement 8. Increasing chromatin stiffness increases mobility globally**: Sweep of
1305 chromatin stiffness by increasing the stiffness of the bond angle potential by up to a factor
1306 two. **(A)** Loci 11kb from the centromere **(B)** Loci 90kb from the centromere. Candidate loci
1307 are selected as in Figure 4 and wild type (WT) refers to the simulation in Figure 4A.

1308 **Figure supplement 9. Combining chromatin stiffness and loosening the kinetochore tether**
1309 **further increases mobility in the pericentromeric region: Sweep of chromatin stiffness as** in
1310 Figure supplement 7 but with a wiggle distance (wd) of 105 nm on the bond connecting the
1311 centromere and the spindle pole body. Candidate loci are 11 kb from the centromere and
1312 selected as in Figure 4. Wild type (WT) refers to the simulation in Figure 4A.

1313 **Figure supplement 10. Smc5-2KE mutation affects HR at pericentromeres without affecting**
1314 **Smc5/6 chromatin loading (A)** I-*Sce*I efficiency (%) after 0h, 2h, 4h and 6h after inducing the
1315 I-*Sce*I with galactose in Smc5 WT and *smc5-2KE* for strains with a DSB at centromeric (C) or
1316 luminal (L) positions. qPCR was done using primers flanking the I-*Sce*I cutting site and actin
1317 was used as a loading control. The error bars represent the standard deviation of three
1318 independent experiments**. (B)** Proportion of cells retaining a centromeric plasmid after
1319 growth in nonselective conditions. Mann-Whitney test was used to analyze differences
1320 between groups, "ns" for not significant. **(C,D)** Chromosomal association of Smc5-MYC and
1321 Smc5-2KE-MYC at selected chromosomal positions as determined by ChIP-qPCR.
1322 Chromosomal positions from the DSB are indicated in the X-axis. Unpaired two-tailed t-test
1323 was used to analyze differences between groups, with "ns" for not significant (P>0.05) and *
1324 for P<0.01. **(E)** I-*Sce*I efficiency (%) of the Smc5 and *smc5-2KE* for C and L strains, used for local
1325 mobility **(F)** MSD as a function of increasing time intervals in the WT and *smc5*-2KE mutant
1326 after inducing a single DSB either at position C or L. Wilcoxon rank-sum test results between
1327 distributions, with the p-value "ns" non-significant, *** (p<0.0001). **(G)** Table summarizing
1328 the different conditions with values extracted from the MSD for the fourth strains used in

1329 local mobility: C WT, C *smc5-2KE,* L WT and L *smc5-2KE*: MSD at 10 sec, the anomalous
1330 exponent (alpha), the sub-diffusive coefficient (D) and the number of cells analyzed.

1331 # Tables

1332 Table 1: genotypes of used strains

Common name	Strain	Genotype	Reference
11kb Chr IV	YPE4019	Mata, ura3, trp1-1, leu2-3, his3-11,15, can1-100, ade2-1, P_{MET3}-CDC20::URA3, Spc42-tdTomato::Nat, leu2:: P_{URA3}-TetR-GFP::LEU2, tetOx224-URA3 (tetOs 11,5kb to right of CEN4), yil015w::KanMX	Paldi *et al* 2020
11kb-2KE Chr IV	YPE4144	Mata, ura3, trp1-1, leu2-3, his3-11,15, can1-100, ade2-1, P_{MET3}-CDC20::URA3, Spc42-tdTomato::Nat, leu2:: P_{URA3}-TetR -GFP::LEU2, tetOx224-URA3 (tetOs 11,5kb to right of CEN4), yil015w::KanMX, YOL034W::K624E, YOL034W::K631E	This study
23kb Chr IV	YEF1659	Mata, ura3, trp1-1, leu2-3, his3-11,15, can1-100, ade2-1, P_{MET3}-CDC20::URA3, Spc42-tdTomato::Nat, leu2:: P_{URA3}-TetR -GFP::LEU2, tetOX224-URA3 (tetOs 11,5kb to right of CEN4)	Paldi *et al* 2020
23kb-2KE Chr IV	YPE4145	Mata, ura3, trp1-1, leu2-3, his3-11,15, can1-100, ade2-1, P_{MET3}-CDC20, Spc42-tdTomato::Nat, leu2:: P_{URA3}-TetR -GFP::LEU2, tetOX224-URA3 (tetOs 23kb to right of CEN4), YOL034W::K624E, YOL034W::K631E	This study
90kb Chr IV	YEF1081	Mat alpha, ura3Δ0 or-851, his3Δ1, can1::HPHMX, his3::HIS3-LacI-GFP, YDR042C::lacO-LEU2	This study
90kb-2KE Chr IV	YEF1654	Mat alpha, ura3Δ0 or-851, his3Δ1, can1::HPHMX, his3::HIS3-LacI-GFP YDR042C::lacO-LEU2, YOL034W::K624E, YOL034W::K631E	This study

730kb Chr IV	YEF1068	Mat alpha, ura3Δ0, leu2Δ0, his3Δ1, lys2Δ202, ade2-661, iyGL117::TetR-mRFP-NATMX, YDR354W::tetO-URA3 HIS3::HIS3-LacI-GFP YDR259C::lacO-TLEU2	This study
730kb-2KE Chr IV	YEF1706	Mat alpha, ura3Δ0, leu2Δ0, his3Δ1lys2Δ202, ade2-661, iyGL117::tetR-mRFP NATMX YDR354W::tetO-URA3 HIS3::HIS3-LacI-GFP, YDR259C::lacO- LEU2, YOL034W::K624E, YOL034W::K631E	This study
90kb-2KR Chr IV	YPE4180	Mat alpha, ura3Δ0, trp1Δ63, leu2Δ0, his3Δ1, lys2Δ202, can1::HPHMX, ade2-661, lys2::TetR-GFP-LYS2, yel053c ::KanMX::tetO-URA3, Chr IV 453880+453959 ::KanMX:: mCherry*-I*Sce*I(cs), YOL034W::K624R, YOL034W::K631ER	This study
90kb Chr V	YEF1454	Mat alpha, ura3Δ0, trp1Δ63, leu2Δ0, his3Δ1, lys2Δ202, can1::HPHMX, ade2-661, lys2::TetR-GFP-LYS2, yel053c ::KanMX:: tetO-URA3, Chr IV 453880+453959 ::KanMX:: mCherry*-I*Sce*I(cs)	García-Fernandez *et al.,* 2022
90kb-2KE Chr V	YEF1666	Mat alpha, ura3Δ0, trp1Δ63, leu2Δ0, his3Δ1, lys2Δ202, can1::HPHMX, ade2-661,::TetR-GFP-LYS2, yel053c ::KanMX:: tetO-URA3, Chr IV 453880+453959 :: KanMX:: mCherry*-I*Sce*I(cs), YOL034W::K624E, YOL034W::K631E	This study
SMC6-AID AFB2	YPE4059	Mat a, trp1-1, leu2-3, his3-11, ade2-1, P_{MET3}-CDC20::URA3, Spc42-tdTomato::Nat, leu2::PURA3::tetR-GFP::LEU2, tetOX224-URA3 (tetOs 11,5kb to right of CEN4), Smc5-AID-9myc-KanMX, his3-11,15 :: pEF604 (=AFB2-HIS3)	This study
SMC1-AID AFB2	YPE4173	Mat a, trp1-1, leu2-3, his3-11, ade2-1, P_{MET3}-CDC20::URA3, Spc42-tdTomato::Nat, leu2::PURA3::tetR-GFP::LEU2, tetOX224-URA3 (tetOs 11,5kb to right of CEN4), yil015w::KanMX, his3-11,15::AFB2-HIS3(pEF604), Smc6-AID-9myc-TRP1	This study
SMC5-AID AFB2	YPE4176	Mat a, trp1-1, leu2-3, his3-11, ade2-1, P_{MET3}-CDC20::URA3, Spc42-tdTomato::Nat, leu2::PURA3::tetR-GFP::LEU2, tetOX224-URA3 (tetOs 11,5kb to right of CEN4), yil015w::KanMX, his3-11,15::AFB2-HIS3(pEF604), Smc1-AID-3myc-TRP1	This study

Rad52 GFP	YEF651	Mata, ura3Δ0, leu2Δ0, his3Δ1, met15Δ0, YML032C-GFP-HIS3MX6	
Rad52-GFP 2KE	YEF1647	Mata, ura3Δ0, leu2Δ0, his3Δ1, met15Δ0, YML032C-GFP-HIS3MX6, YOL034W::K624E, YOL034W::K631E	This study
RAD53-HA	YEF954	Mat alpha, ura3-Δ851, trp1-Δ63, leu2Δ1, his3Δ200, ade2-661, yml032c::KANMX, rad53-HA	
RAD53-HA 2KE	YEF1882	Mat alpha, ura3-Δ851, trp1-Δ63, leu2Δ1, his3Δ200, ade2-661, yml032c::KANMX, rad53-HA, YOL034W::K624E, YOL034W::K631E	This study
R1	YEF1065	Mat a, ura3Δ0, leu2Δ0/, his3Δ1, lys2Δ202, ade2-661, can1::HPHMX, iyGL117::tetR-mRFP- NATMX, YDR003W::tetO-TEF-URA, HIS3::HIS3-LacI-GFP, YDR095C::256lacO-TEF-LEU2	Herbert *et al* 2017
R1 2KE	YEF1887	Mat a, ura3Δ0, leu2Δ0/, his3Δ1, lys2Δ202, ade2-661, can1::HPHMX, iyGL117::tetR-mRFP- NATMX, YDR003W::tetO-TEF-URA, HIS3::HIS3-LacI-GFP, yDR095c::256lacO-LEU2, YOL034W::K624E, YOL034W::K631E	This study
R3	YEF1068	Mat alpha, ura3Δ0, leu2Δ0, his3Δ1, lys2Δ202, ade2-661, iyGL117::tetR-mRFP-NATMX, YDR354W::tetO-TEF-URA3 HIS3::HIS3-LacI-GFP YDR259C::lacO- LEU2	Herbert *et al* 2017
R3 2KE	YEF1706	Mat alpha, ura3Δ0, leu2Δ0, his3Δ1, lys2Δ202, ade2-661, iyGL117::tetR-mRFP NATMX YDR354W::tetO-TEF-URA3 HIS3::HIS3-LacI-GFP YDR259C::lacO- LEU2, YOL034W::K624E, YOL034W::K631E	This study
Tub2-GFP	YPE257	Mata, ura3-52, trp1Δ63, leu2Δ1, lys2-801, ade2-661, ura3-52::TUB2-GFP-URA3	
Tub2-GFP SMC5-2KE	YEF1864	Mata, ura3-52, trp1Δ63, leu2Δ1, lys2-801, ade2-661, ura3-52::TUB2-GFP-URA3, YOL034W::K624E, YOL034W::K631E	This study

Smc5-ndc80-1	YEF1928	Mat alpha, ura3Δ0, trp1Δ63, leu2Δ0, his3Δ1, lys2Δ202, can1::HphMX,ade2-661, lys2::TetR-GFP-LYS2, yel053c ::KanMX:: tetO-URA3, Chr IV 453880+453959::KanMX:: mCherry*-I-*Sce*I(cs), ndc80-1	This study
ndc80-1 Smc5-2KE	YEF1930	Mat alpha, ura3Δ0, trp1Δ63, leu2Δ0, his3Δ1, lys2Δ202, can1::HphMX,ade2-661/,lys2::TetR-GFP-LYS2, yel053c ::KanMX:: tetO-URA3, Chr IV 453880+453959::KanMX:: mCherry*-I-*Sce*I(cs), YOL034W::K624E, YOL034W::K631E, ndc80-1	This study
L WT sDSB	YEF1203	Mat alpha, ura3Δ0, trp1Δ63, leu2Δ0, his3Δ1, lys2Δ202, ade2-661, lys2::TetR-GFP-LYS2, can1::HphMX, YEL053C :: KANMX:: tetO-URA Chr IV 853996+854075:: KANMX:: mCherry*-I-*Sce*I(cs)	García-Fernandez *et al.,* 2022
L 2KE sDSB	YPE4131	Mat alpha, ura3Δ0, trp1Δ63, leu2Δ0, his3Δ1, lys2Δ202, ade2-661, lys2::TetR-GFP-LYS2, can1::HPHMX, YEL053C::KanMX::tetO-URA, Chr IV 853996+854075:: KanMX:: mCherry*-I-*Sce*I(cs), YOL034W::K624E, YOL034W::K631E,	This study
C - DSB Local mobility	YPE4132	Mata,ura3Δ0,,leu2Δ0/,his3Δ1/, met15Δ0/,YOL034W-13xMYC-URA3, Chr IV 453880+453959::KanMX::mCherry*-I*Sce*I(cs), ymr008C::KanMX::lacO-LEU2, LacI-HIS3, HIS3-STOP, p2u-HIS3	This study
C + DSB Local mobility	YPE4133	Mata, ura3Δ0, leu2Δ0, his3Δ1, met15Δ0, YOL034W-13xMYC-URA3, Chr IV 453880+453959::KANMX::mCherry*-I-*Sce*I(cs), ymr008C::kanMX::lacO-LEU2, LacI-HIS3, HIS3-STOP, pGALISceI-HIS3	This study
C 2KE - DSB Local mobility	YPE4136	Mata, ura3Δ0, leu2Δ0, his3Δ1, met15Δ0, YOL034W::K624E, YOL034W::K631E, YOL034W-13xMYC-URA3, Chr IV 453880+453959::KanMX: mCherry*-I-*Sce*I(cs), ymr008C::kanMX::lacO-LEU2, LacI-HIS3, HIS3-STOP, p2u-HIS3	This study

C 2KE + DSB Local mobility	YPE4137	Mata, ura3Δ0, leu2Δ0, his3Δ1, met15Δ0, YOL034W::K624E, YOL034W::K631E, YOL034W-13xMYC-URA3, Chr IV 453880+453959::KanMX::mCherry*-I-*Sce*I(cs), ymr008C::kanMX::lacO-LEU2, LacI-HIS3, HIS3-STOP, pGALISceI-HIS3	This study
L - DSB sDSB Local mobility	YPE4134	Mata, ura3Δ0, leu2Δ0, his3Δ1, met15Δ0, YOL034W-13xMYC-URA3, Chr IV 853996+854075::KanMX::mCherry*-I-*Sce*I(cs), ydr193w::kanMX::lacO-LEU2, LacI-HIS3, HIS3-STOP, p2u-HIS3	This study
L + DSB Local mobility	YPE4135	Mata, ura3Δ0, leu2Δ0, his3Δ1, met15Δ0, YOL034W-13xMYC-URA3, Chr IV 853996+854075::KanMX::mCherry*-I-*Sce*I(cs), ydr193w::kanMX::lacO-LEU2, LacI-HIS3, HIS3-STOP, pGALISceI-HIS3	This study
L 2KE - DSB Local mobility	YPE4138	Mata, ura3Δ0, leu2Δ0, his3Δ1, met15Δ0, YOL034W::K624E, YOL034W::K631E, YOL034W-13xMYC-URA3, Chr IV 853996+854075::KanMX::mCherry*-I-*Sce*I(cs), ydr193w::kanMX::lacO-LEU2, LacI-HIS3, HIS3-STOP, p2u-HIS3	This study
L 2KE + DSB Local mobility	YPE4139	Mata, ura3Δ0, leu2Δ0, his3Δ1, met15Δ0, YOL034W::K624E, YOL034W::K631E, YOL034W-13xMYC-URA3, Chr IV 853996+854075::KanMX::mCherry*-I-*Sce*I(cs), ydr193w::kanMX::lacO-LEU2, LacI-HIS3, HIS3-STOP, pGALISceI-HIS3	This study
C - DSB ChIP-qPCR	YEF1922	Mata, ura3Δ0, leu2Δ0, his3Δ1, met15Δ0, YOL034W-13xMYC-URA3, Chr IV 853996+854075:: kanMX::mCherry*-ISceI(cs), p2u-HIS3	This study
C + DSB ChIP-qPCR	YEF1923	Mata, ura3Δ0, leu2Δ0, his3Δ1, met15Δ0, YOL034W-13xMYC-URA3, Chr IV 853996+854075::kanMX:::mCherry*-I-*Sce*I(cs), pGALISceI-HIS3	This study
C 2KE - DSB ChIP-qPCR	YEF1934	Mata, ura3Δ0, leu2Δ0, his3Δ1, met15Δ0, YOL034W::K624E, YOL034W::K631E, YOL034W-13xMYC-URA3, Chr IV 453880+453959 :: kanMX :: mCherry*-I-*Sce*I(cs), p2u-HIS3	This study

C 2KE + DSB ChIP-qPCR	YEF1925	Mata, ura3Δ0, leu2Δ0, his3Δ1, met15Δ0, YOL034W::K624E, YOL034W::K631E, YOL034W-13xMYC-URA3, Chr IV 453880+453959 :: kanMX :: mCherry*-I-*Sce*I(cs), $P_{GAL1-10}$-*I-SceI*-HIS3	This study
L - DSB ChIP-qPCR	YEF1898	Mata, ura3Δ0, leu2Δ0, his3Δ1, met15Δ0, YOL034W-13xMYC-URA3, Chr IV 853996+854075:: kanMX :: mCherry*-I-*Sce*I(cs), p2u-HIS3	This study
L + DSB ChIP-qPCR	YEF1900	Mata, ura3Δ0, leu2Δ0, his3Δ1, met15Δ0, YOL034W-13xMYC-URA3, Chr IV 853996+854075::kanMX::mCherry*-I-*Sce*I(cs), $P_{GAL1-10}$-*I-SceI*-HIS3	This study
L 2KE - DSB ChIP-qPCR	YEF1926	Mata, ura3Δ0, leu2Δ0, his3Δ1, met15Δ0, YOL034W::K624E, YOL034W::K631E, YOL034W-13xMYC-URA3, Chr IV 853996+854075::kanMX::mCherry*-I-*Sce*I(cs), p2u-HIS3	This study
L 2KE + DSB ChIP-qPCR	YEF1920	Mata, ura3Δ0, leu2Δ0, his3Δ1, met15Δ0, YOL034W::K624E, YOL034W::K631E, YOL034W-13xMYC-URA3, Chr IV 853996+854075::kanMX::mCherry*-*I-SceI*(cs), $P_{GAL1-10}$-*I-SceI*-HIS3	This study
CEN-SPB	YEF1019	Mat a, his3Δ1 or his3Δ200, lys2Δ202 or 0, cenIV-tetO-URA3, lys2Δ202::tetR-GFP-LYS2 , SPC42-mCherry-HIS3	García-Fernandez *et al.,* 2021
CEN-SPB Smc5-2KE	YEF1691	Mat a, his3Δ1 or his3Δ200, lys2Δ202 or 0, cenIV-tetO-URA3, lys2Δ202::tetR-GFP-LYS2 , SPC42-mCherry-HIS3, YOL034W::K624E, YOL034W::K631E	This study
Mtw1-3xGFP	YEF1017	Mat a, ura3-1, trp1-1, leu2Δ3,112, his3-11, can1-100, ade2-1, ura3::TUB1-CFP::URA3, YAL034W-A-3xGFP::HIS3, yil015w::KANMX	García-Fernandez *et al.,* 2021
Mtw1-3xGFP Smc5-2KE	YEF4025	Mat a, ura3-1, trp1-1, leu2Δ3,112, his3-11, can1-100, ade2-1, ura3::TUB1-CFP::URA3, YAL034W-A-3xGFP::HIS3, YOL034W::K624E, YOL034W::K631E, yil015w::KANMX	This study

SMC5-3xSTII, CBP-9xHIS-SMC6	D10079	Mata, W303, ura3-1, trp1-1, leu2-3,112, his3-11,15, can1-100, ade2-1, [PSI+], rad5-535, SMC5-3xSTII::TRP1, CBP-9xHIS-SMC6	This study

Table 2: primers used in this study

Gene / region	Primer	Sequence (5'⍰ 3')	Reference
gRNA 2KE	oACS13	CTGAAGGGCGAGATCAAGCgtttt	This study
	oACS14	CTCGTTGTGGGAGGTGATGTgatca	This study
Donor 2KE	oACS69	TCATGGGAATAGGTTAGTCGATATC**GAA**CAATCAGCATATGGTAGTgaaCAGGTCTTTCCTACTGACGTTAGTATTAAAC	This study
Donor 2KA	oACS97	TCATGGGAATAGGTTAGTCGATATC**GCG**CAATCAGCATATGGTAGT**GCG**CAAGTCTTTCCTACTGACGTTAGTATTAAAC	This study
Donor 2KR	oACS270	TCATGGGAATAGGTTAGTCGATATC**AGA**CAATCAGCATATGGTAGT**AGA**CAAGTCTTTCCTACTGACGTTAGTATTAAAC	This study
Smc5-MYC	oACS103	ATCCGAAGATGATACATTTCGGTGAAACTTCTAACTACTCATTCGAACGGATCCCCGGGttaattaa	This study
	oACS94	AAACATGTTTACATCTATATGTGTATAATTAATTATGCAATAGTGAAAGATGAATTCGAGCTCGTTTAAAC	This study
AID	oACS40	AGGATCCGAAGATGATACATTTCGGTGAAACTTCTAACTACTCATTCGATcgtacgctgcaggtcgac	This study

	oACS53	AAACATGTTTACATCTATATGTGTATAATTAATTATGCAATAGTGAAAGAatcgatgaattcgagctcg	This study
AFB2	oACS199	ACGCGCCGCTCACCCGCACGGCAGAGACCAATCAGTAAAAATCAACGGTTAATTCGGTCGAAAAAAGAAA	This study
	oACS200	AGCTTACATTTTATGTTAGCTGGTGGACTGACGCCAGAAAATGTTGGTGATTAGAGAATCCACACAAATG	This study
KanMX R1	OEA177	ACTTGGTTGGCGTGTTTCGT	This study
	OEA178	GCGGTTGTTTGCAAGACCGA	This study
KanMX R2	OEA181	GTCAAGGGCGTGTTTGACGC	This study
	OEA182	ACGAATTTTGCTCCGGCAATTCT	This study
Cherry -*I-SceI*- cs	OEA310	TAGGATACAGTTCTCACATCACATCCGAACATAAACAACCATGGTGAGCAAGGGCGA	This study
	OEA311	ATGACAAGTTCTTGAAAACAAGAATCTTTTTATTGTCAGTCTACTTGTACAGCTCGTCCATG	This study
gRNA HIS3	oACS13	GAGTGCGTTCAAGGCTCTTGgtttt	This study
	oACS14	CAAGAGCCTTGAACGCACTCgatca	This study
Donor HIS3	oACS69	GATTAACGTCCACACAGGTATAGGGTTTCTGGACCATATGATA**TAA**GCTCTGGCCAAGCATT CCGGCTGGTCGCTAATCG	This study
R1 5 Kb		GGCAATTGAGGCCTTCTGGC	García Fernandez et al., 2021
		TGGTGGCCAACGATCCTTCA	

R1 10Kb	oACS136	AGCGGAATCAGGAGTGCAAAA	This study
	oACS137	TGGAAAAATGCATCTACAACCGCT	
R1 15 Kb	oACS138	GCCAAAGGTGTTTTCATTTGGAAGG	This study
	oACS139	ACCAGCACCTGACTCTCCCA	
R1 50 Kb		TTCTCCCTTGTCACCGCCACC	García Fernandez et al., 2021
		GGCCGCTCAAGTTAACGCCCA	
R1 150 Kb		TGGGAATCGTTTTATCCTTGTTTCGC	García Fernandez et al., 2021
		GTGAAGCAACCAACATAATGCCAG	
	oACS194	ACGCGAGGATTTTTGTTCGTGG	

1335

1336 Table 3: plasmids used in this study

Name	**Marker**	**Features**	**Origin**

pEF562	KANMX	Plasmid carrying Cas9 and a gRNA scaffold. gRNAs were introduced by digesting this plasmid with BplI.	[87]
pEF590	KANMX	Plasmid coming from the pEF562 carrying the gRNA to cut close to the SMC5-K631.	This study
pEF601	URA3	Plasmid carrying pFA6a-13MYC-URA3 used to introduce 13x MYC at the C-terminus of *SMC5*	P. Lesage
pEF222	LEU2	Plasmid carrying pTEF-tTEF-LEU2-LacO, used to integrate the LacO in the place of a KanMX	Therizols et al., 2010
pEF569	HIS3	Plasmid carrying LacI-GFP-HIS3, which was linearized with *NheI* to introduce LacI-GFP into *HIS3*	
pEF604	HIS3	Plasmid carrying the AFB2, which was linearized with *NheI* to introduce AFB2-URA3 into *URA3*.	T. Teixeira
pEF608	HIS3	Plasmid coming from the pJH2970 (Addgene, 100954) carrying the gRNA to cut close to the Smc5-K631.	This study
pB07	HIS3	Plasmid carrying the I-*Sce*I enzyme under GAL1-10 promoter	García-Fernandez et al 2022
pEF573	ADE2	Centromeric plasmid carrying the mCherry donor sequence, without the promoter and terminator.	García-Fernandez et al 2022

1337

1338 References cited in methods

1339

1340 81. Adhikary, H., & D'Amours, D. (2025). Production and Purification of the Human SMC5/6
1341 Core Complex from S. cerevisiae (Vol. 2991). Springer US
1342 82. Nishimura, K. & Kanemaki, M. T. Rapid Depletion of Budding Yeast Proteins via the
1343 Fusion of an Auxin-Inducible Degron (AID). *Curr Protoc Cell Biol* 64, 20.9.1-20.9.16 (2014).
1344 83. Morawska, M. & Ulrich, H. D. An expanded tool kit for the auxin-inducible degron system
1345 in budding yeast. *Yeast* 30, 341–351 (2013).
1346 84. Ratsima, H. *et al.* Independent modulation of the kinase and polo-box activities of Cdc5
1347 protein unravels unique roles in the maintenance of genome stability. *Proc Natl Acad Sci*
1348 *U S A* 108, (2011).
1349 85. Livak, K. J. & Schmittgen, T. D. Analysis of Relative Gene Expression Data Using Real-Time
1350 Quantitative PCR and the 2−ΔΔCT Method. *Methods* 25, 402–408 (2001).
1351 86. Liu, S. *et al.* In vivo tracking of functionally tagged Rad51 unveils a robust strategy of
1352 homology search. *Nat Struct Mol Biol* 30, 1582–1591 (2023).
1353 87. Arbona, J. M., Herbert, S., Fabre, E. & Zimmer, C. Inferring the physical properties of
1354 yeast chromatin through Bayesian analysis of whole nucleus simulations. *Genome Biol* 18,
1355 (2017).
1356 88. Eastman, P. *et al.* OpenMM 7: Rapid development of high performance algorithms for
1357 molecular dynamics. *PLoS Comput Biol* 13, e1005659 (2017).
1358

Figure. 1

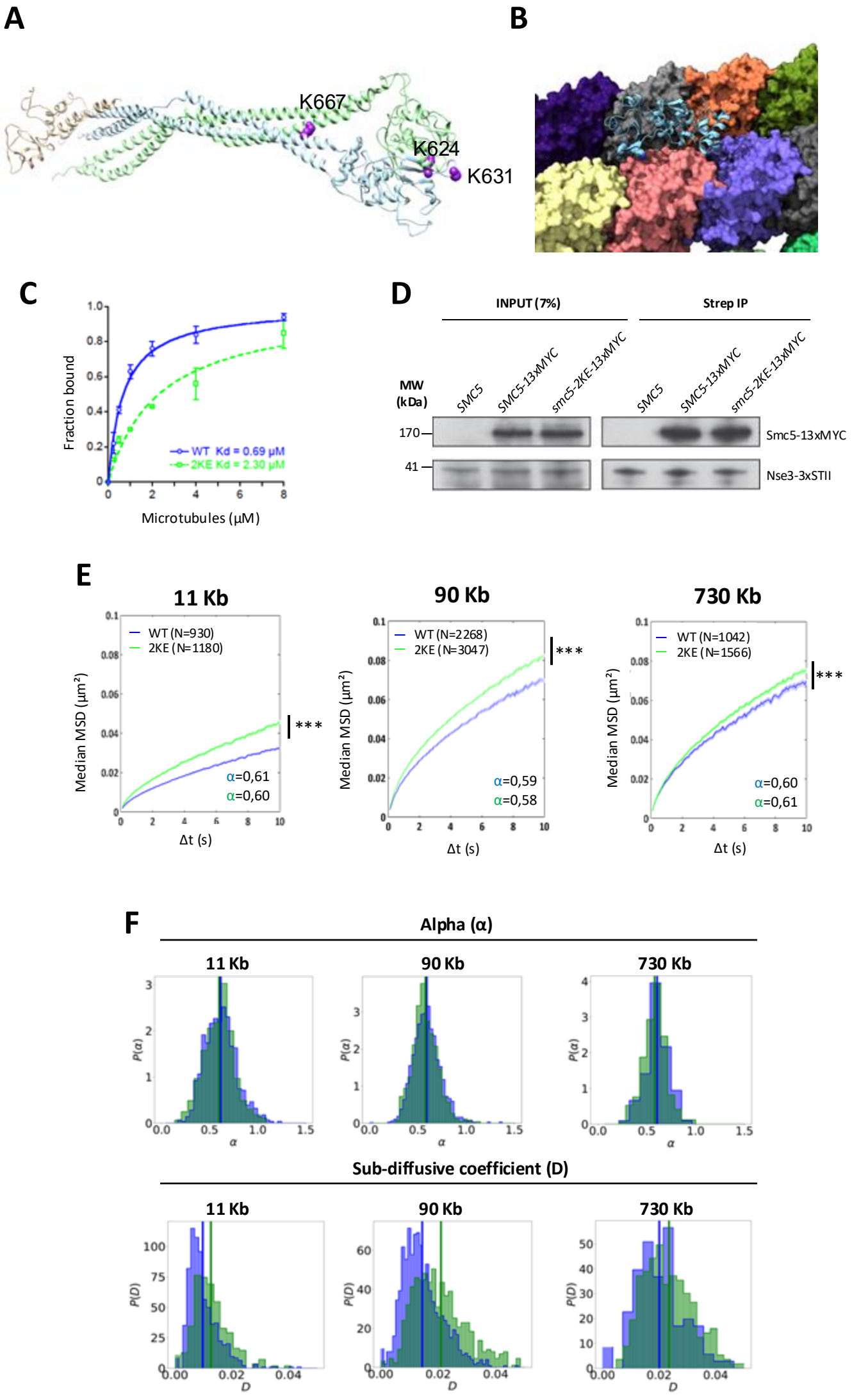
A
K667
K624
K631
B
C
Fraction bound
Microtubules (µM)
WT Kd = 0.69 µM
2KE Kd = 2.30 µM
D
INPUT (7%)
Strep IP
MW (kDa)
SMC5
SMC5-13xMYC
smc5-2KE-13xMYC
170
41
Smc5-13xMYC
Nse3-3xSTII
E
11 Kb
90 Kb
730 Kb
WT (N=930)
2KE (N=1180)
WT (N=2268)
2KE (N=3047)
WT (N=1042)
2KE (N=1566)
Median MSD (µm²)
Δt (s)
α=0,61
α=0,60
α=0,59
α=0,58
α=0,60
α=0,61
***
F
Alpha (α)
P(α)
α
Sub-diffusive coefficient (D)
P(D)
D

Figure 2

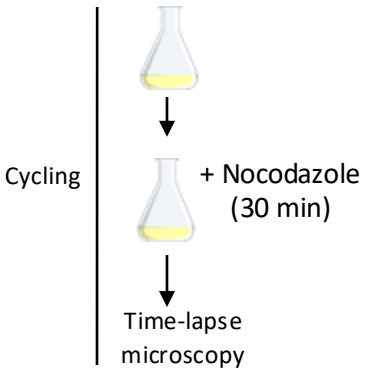

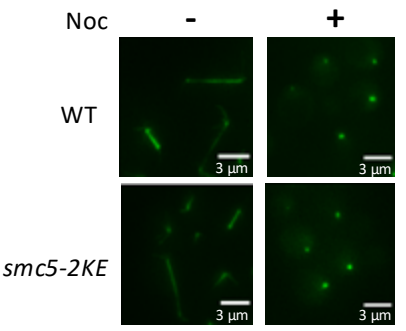

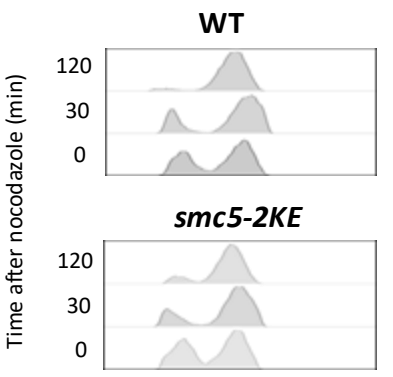

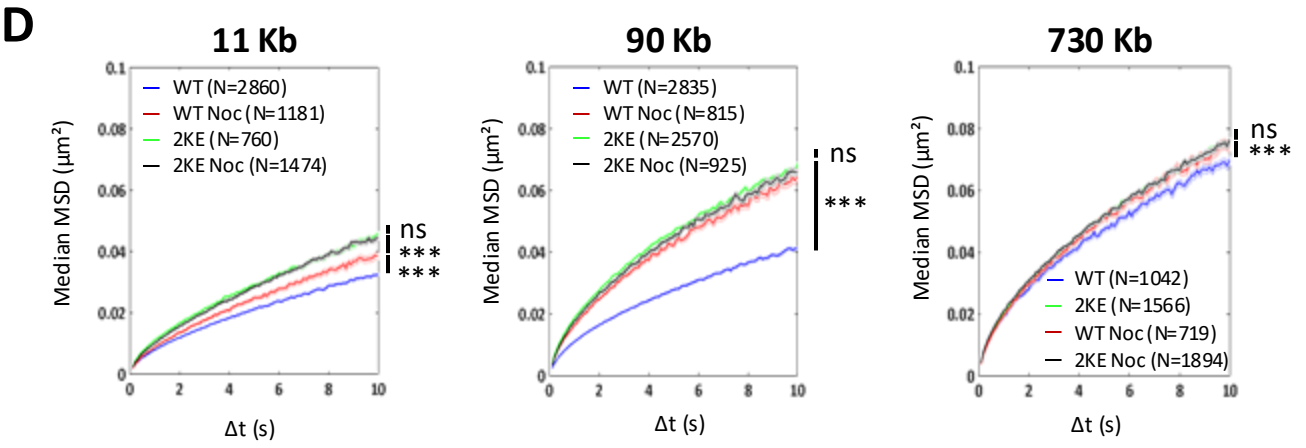

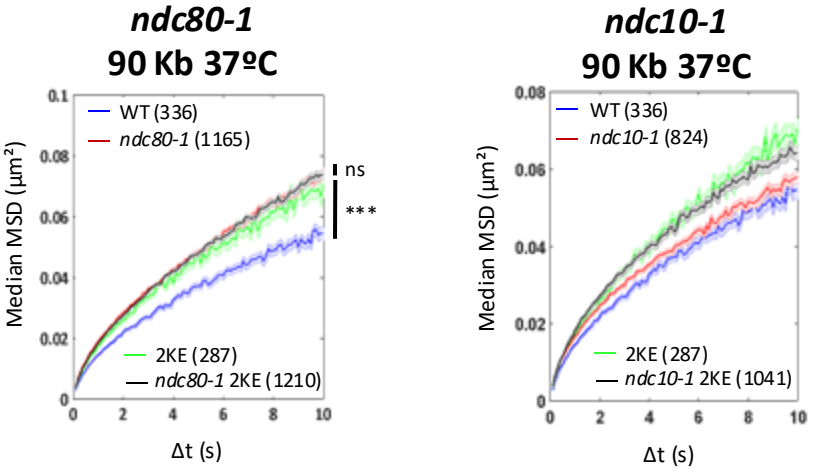

F

Cell phase	Tracked locus	Smc5 allele	MSD at 10 sec (10^{-2})	Alpha	D (10^{-3})	Cell number
Cycling + Nocodazole	11 kb	**WT**	3.83	0.62	2.19	760
		smc5-2KE	4.45	0.62	2.54	1474
	90 kb	**WT**	6.47	0.61	2.00	815
		smc5-2KE	6.58	0.60	2.70	925
	730 kb	**WT**	7.44	0.60	4.71	719
		smc5-2KE	7.63	0.58	5.07	1894
Cycling 37ºC	90 kb	**WT**	5.43	0.60	3.49	336
		ndc80-1	7.49	0.61	4.42	1165
		smc5-2KE	7.04	0.60	4.59	287
		ndc80-1 smc5-2KE	7.38	0.61	4.46	1210

Figure 3

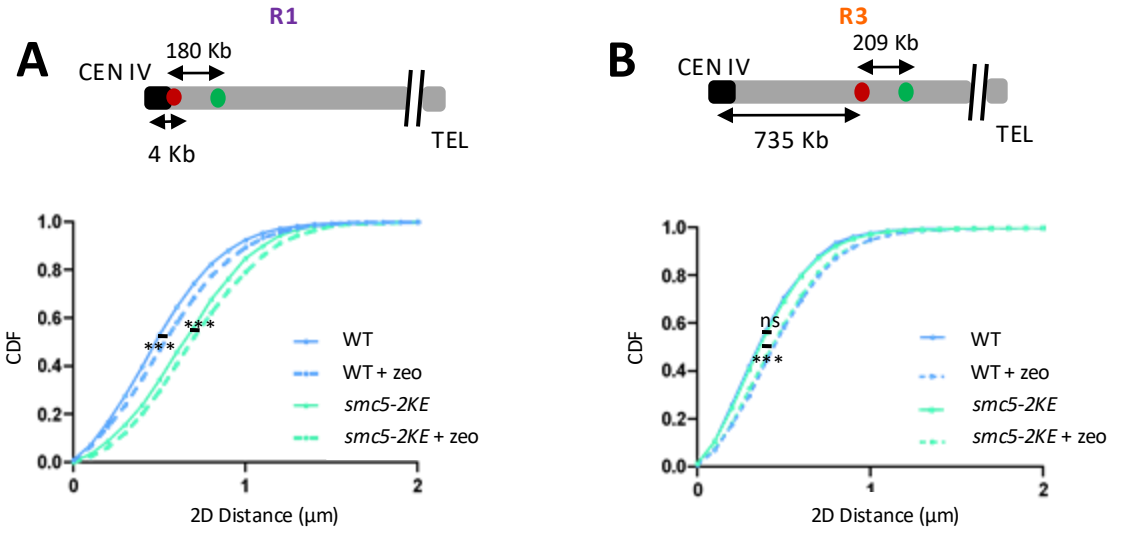

Figure 4

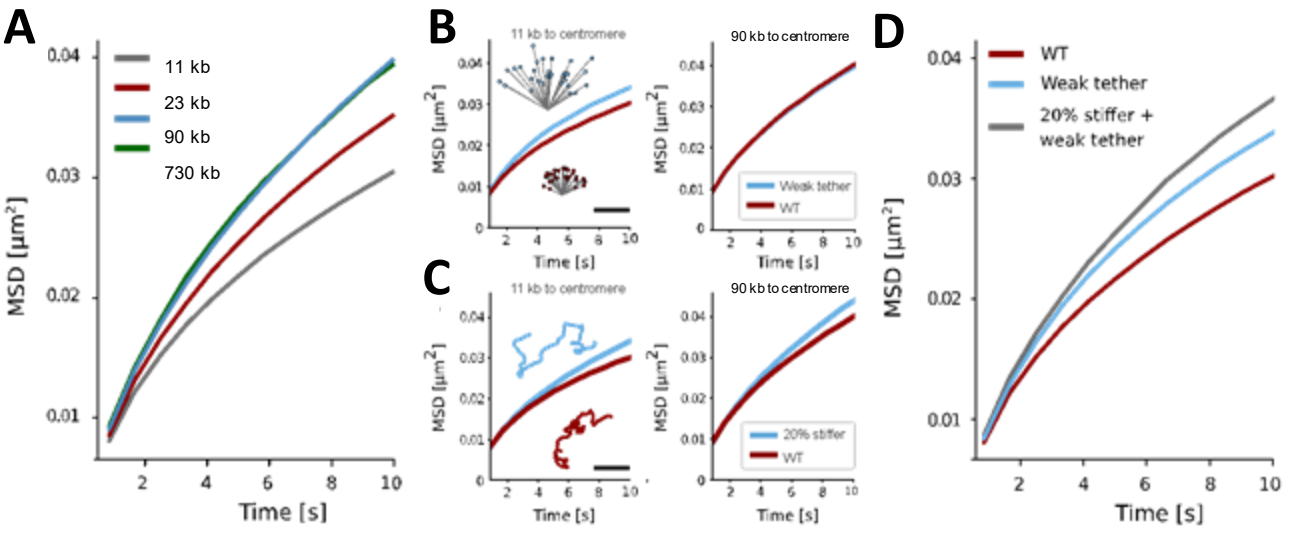

Figure 5

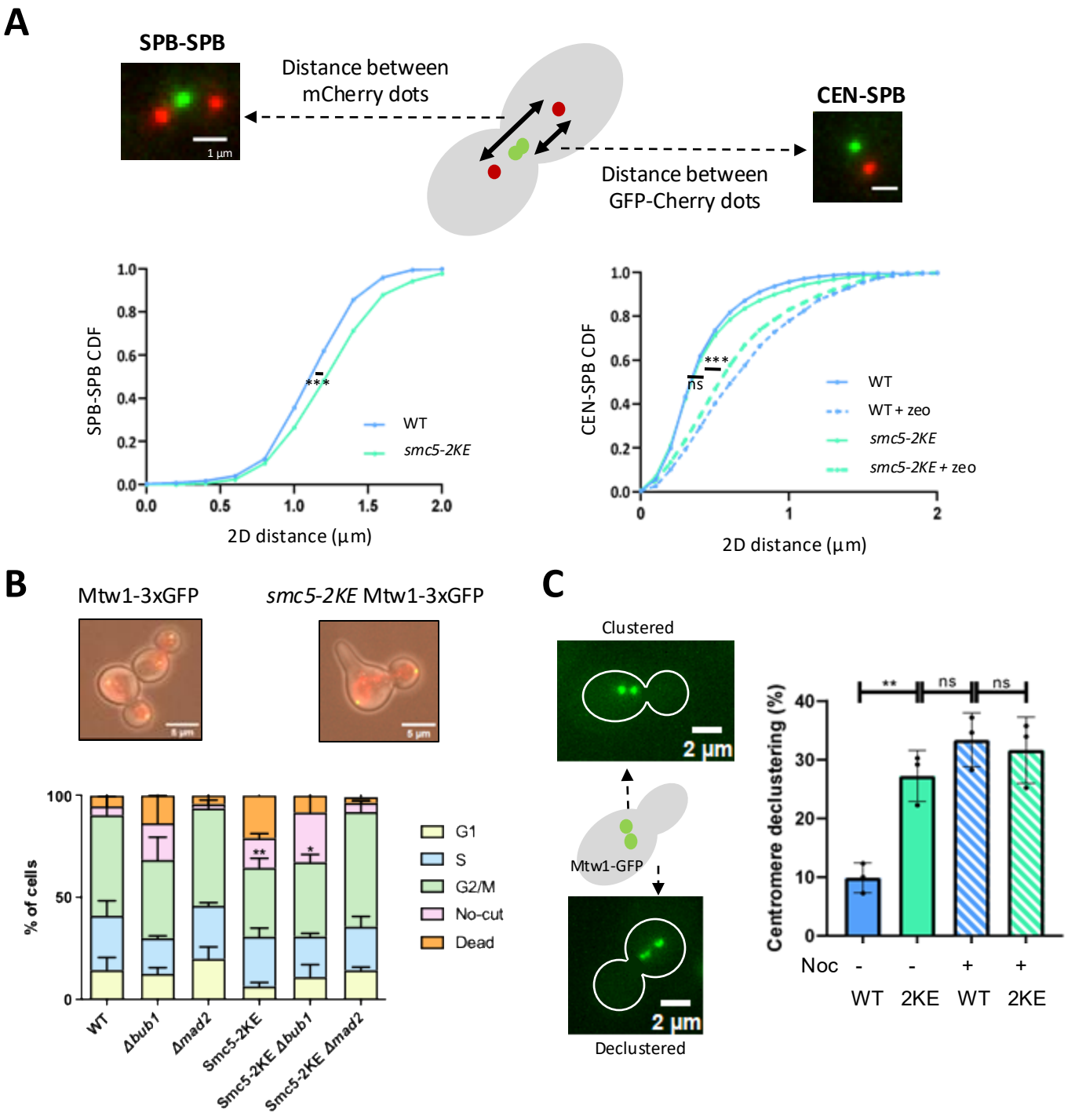
A
SPB-SPB
1 µm
Distance between mCherry dots
CEN-SPB
Distance between GFP-Cherry dots
SPB-SPB CDF
2D distance (µm)
***
WT
smc5-2KE
CEN-SPB CDF
ns
***
WT
WT + zeo
smc5-2KE
smc5-2KE + zeo
2D distance (µm)
B
Mtw1-3xGFP
smc5-2KE Mtw1-3xGFP
% of cells
G1
S
G2/M
No-cut
Dead
WT
Δbub1
Δmad2
Smc5-2KE
Smc5-2KE Δbub1
Smc5-2KE Δmad2
C
Clustered
2 µm
Mtw1-GFP
2 µm
Declustered
Centromere declustering (%)
**
ns
ns
Noc
WT
2KE
WT
2KE

Figure 6

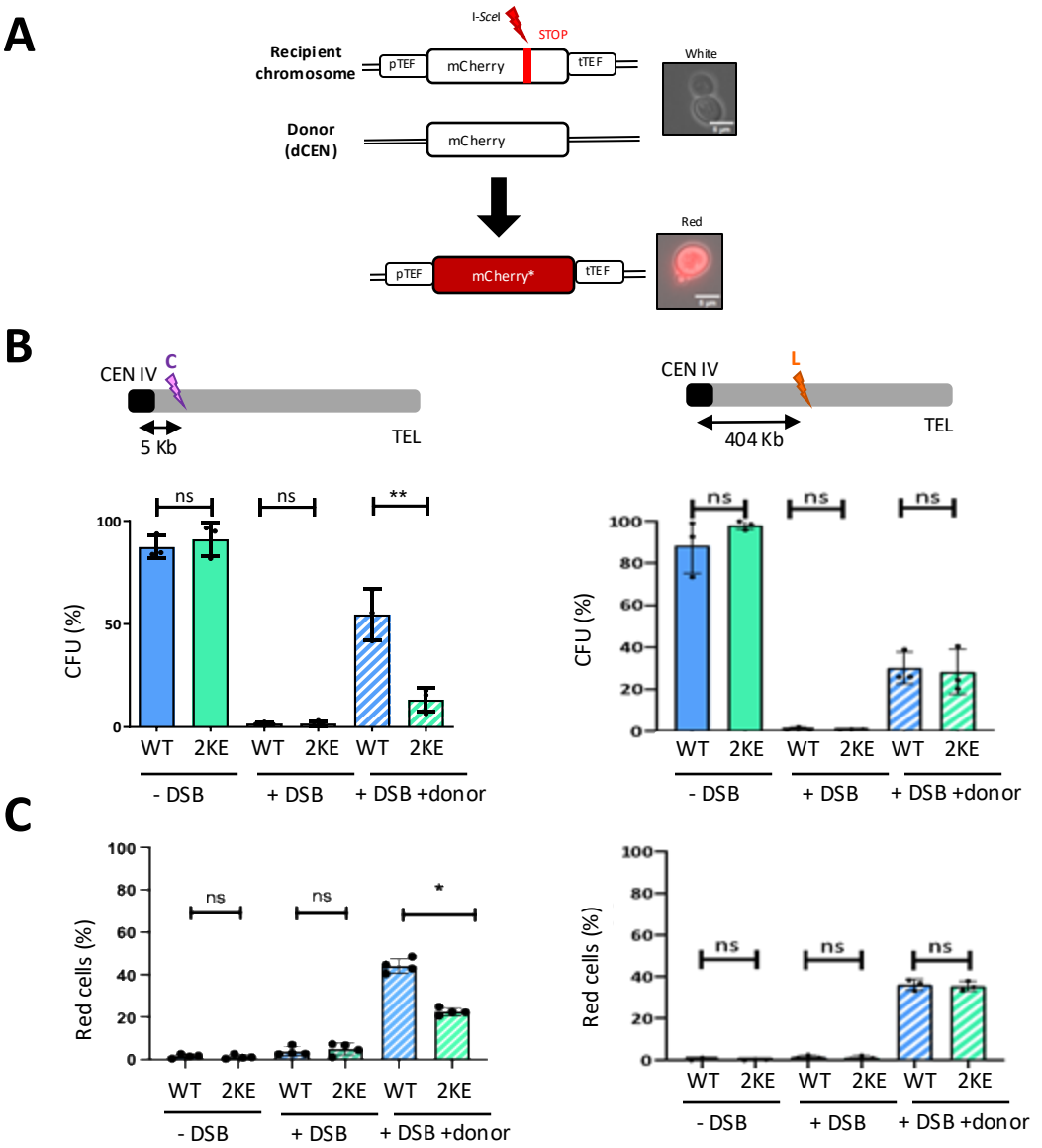
A
I-SceI
STOP
Recipient chromosome
pTEF
mCherry
tTEF
White
Donor (dCEN)
mCherry
Red
pTEF
mCherry*
tTEF
B
CEN IV
C
5 Kb
TEL
CEN IV
L
404 Kb
TEL
CFU (%)
ns
ns
**
WT
2KE
WT
2KE
WT
2KE
- DSB
+ DSB
+ DSB +donor
CFU (%)
ns
ns
ns
C
Red cells (%)
ns
ns
*
Red cells (%)
ns
ns
ns

Figure supplement 1

A

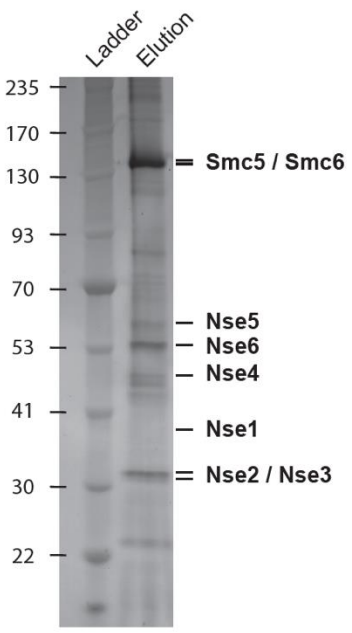

B

Tubulin Beta Chain – *Saccharomyces cerevisiae*

```
M R E I I H I S T G   Q C G N Q I G A A F   W E T I C G E H G L   D F N G T Y H G H D
D I Q K E R L N V Y   F N E A S S G K W V   P R S I N V D L E P   G T I D A V R N S A
I G N L F R P D N Y   I F G Q S S A G N V   W A K G H Y T E G A   E L V D S V M D V I
R R E A E G C D S L   Q G F Q I T H S L G   G G T G S G M G T L   L I S K I R E E F P
D R M M A T F S V L   P S P K T S D T V V   E P Y N A T L S V H   Q L V E H S D E T F
C I D N E A L Y D I   C Q R T L K L N Q P   S Y G D L N N L V S   S V M S G V T T S L
R Y P G Q L N S D L   R K L A V N L V P F   P R L H F F M V G Y   A P L T A I G S Q S
F R S L T V P E L T   Q Q M F D A K N M M   A A A D P R N G R Y   L T V A A F F R G K
V S V K E V E D E M   H K V Q S K N S D Y   F V E W I P N N V Q   T A V C S V A P Q G
L D M A A T F I A N   S T S I Q E L F K R   V G D Q F S A M F K   R K A F L H W Y T S
E G M D E L E F S E   A E S N M N D L V S   E Y Q Q Y Q E A T V   E D D E E V D E N G
D F G A P Q N Q D E   P I T E N F E
```

C

Peptide sequences	Probability
(R)SINVDLEPGTIDAVR(N)	**100%**
(R)YPGQLNSDLR(K)	**98%**
(K)LAVNLVPFPR(L)	**98%**

Figure supplement 2

A

Smc5 Region	Interacting Protein	Protein Complex	ipTM	pTM	Confidence
450–645	Shs1	Septin complex	0.18	0.48	Low
450–645	Actin	Actin cytoskeleton	0.16	0.8	Low
450–645	Tub1/Tub2	Microtubule (α/β-tubulin)	0.72	0.8	High

B

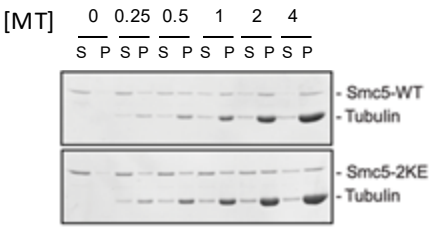

C

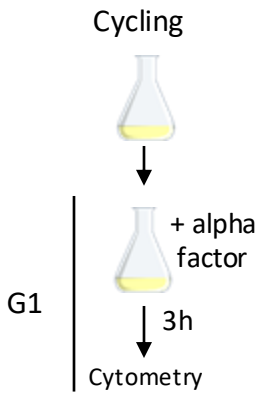

D

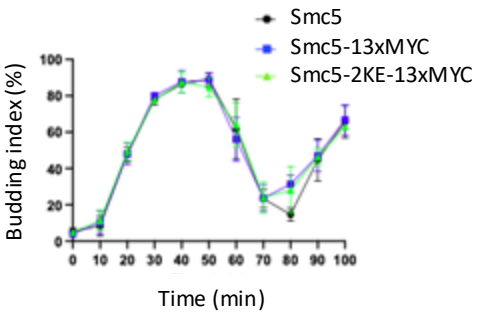

E

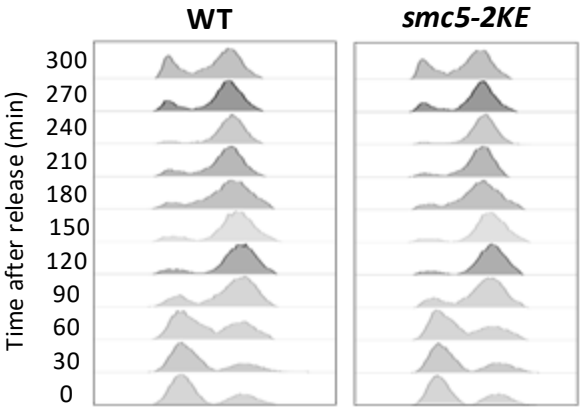

F

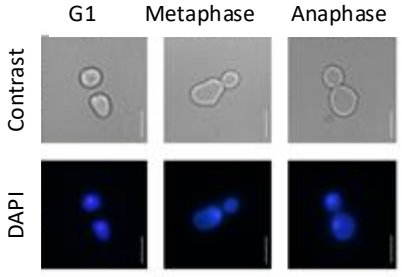

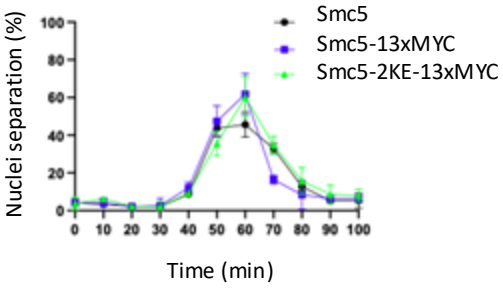

G

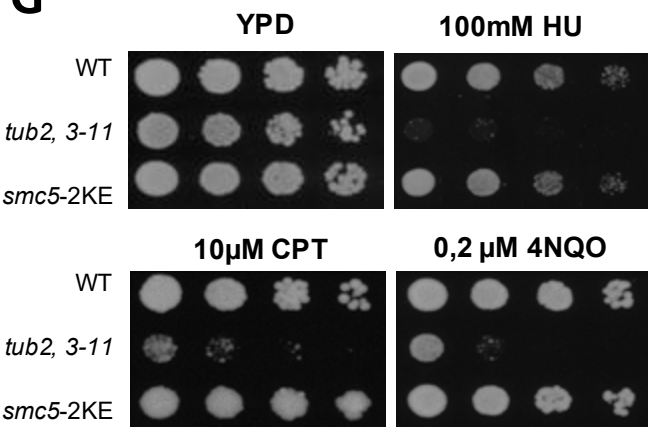

H

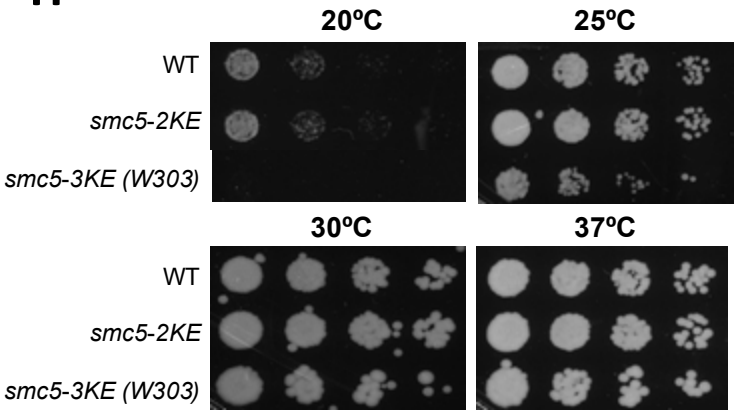

I

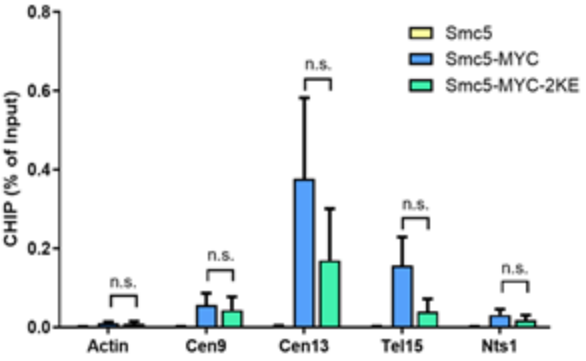

Figure supplement 3

A

Tracked locus	Smc5 allele	MSD at 10 sec (10^{-2})	Alpha	D (10^{-3})	Cell number
11 kb	WT	3.35	0.61	2.0	930
	smc5-2KE	4.57	0.60	2.7	1180
90 kb	WT	6.97	0.59	2.9	2268
	smc5-2KE	8.25	0.58	3.3	3047
730 kb	WT	6.97	0.60	4.8	1042
	smc5-2KE	7.52	0.61	5.2	1566
90 kb	*smc5-2KE*	7,63	0.62	4.4	1557
	smc5-2KR	6.49	0.61	4.0	1290

C

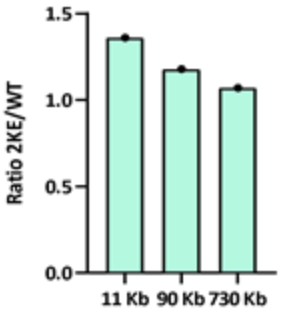

D

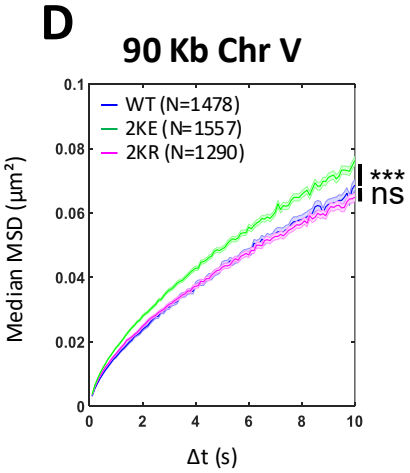

B

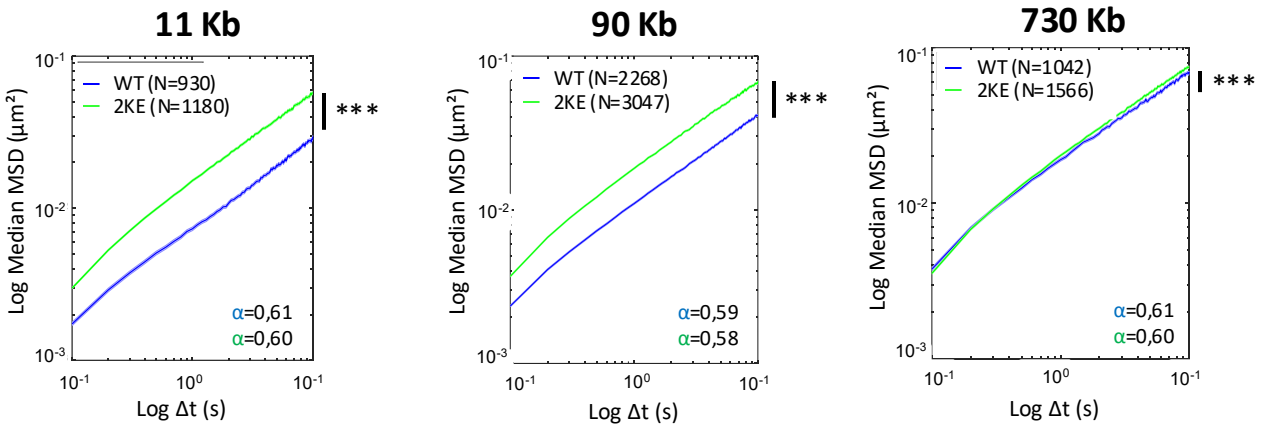

E

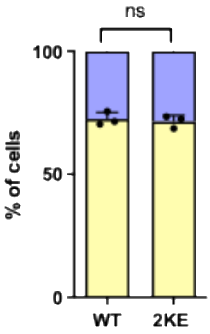

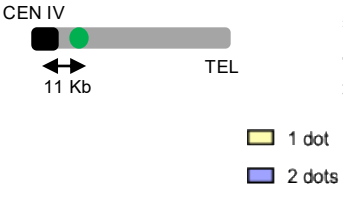

F

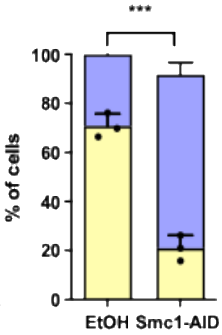

Figure supplement 4

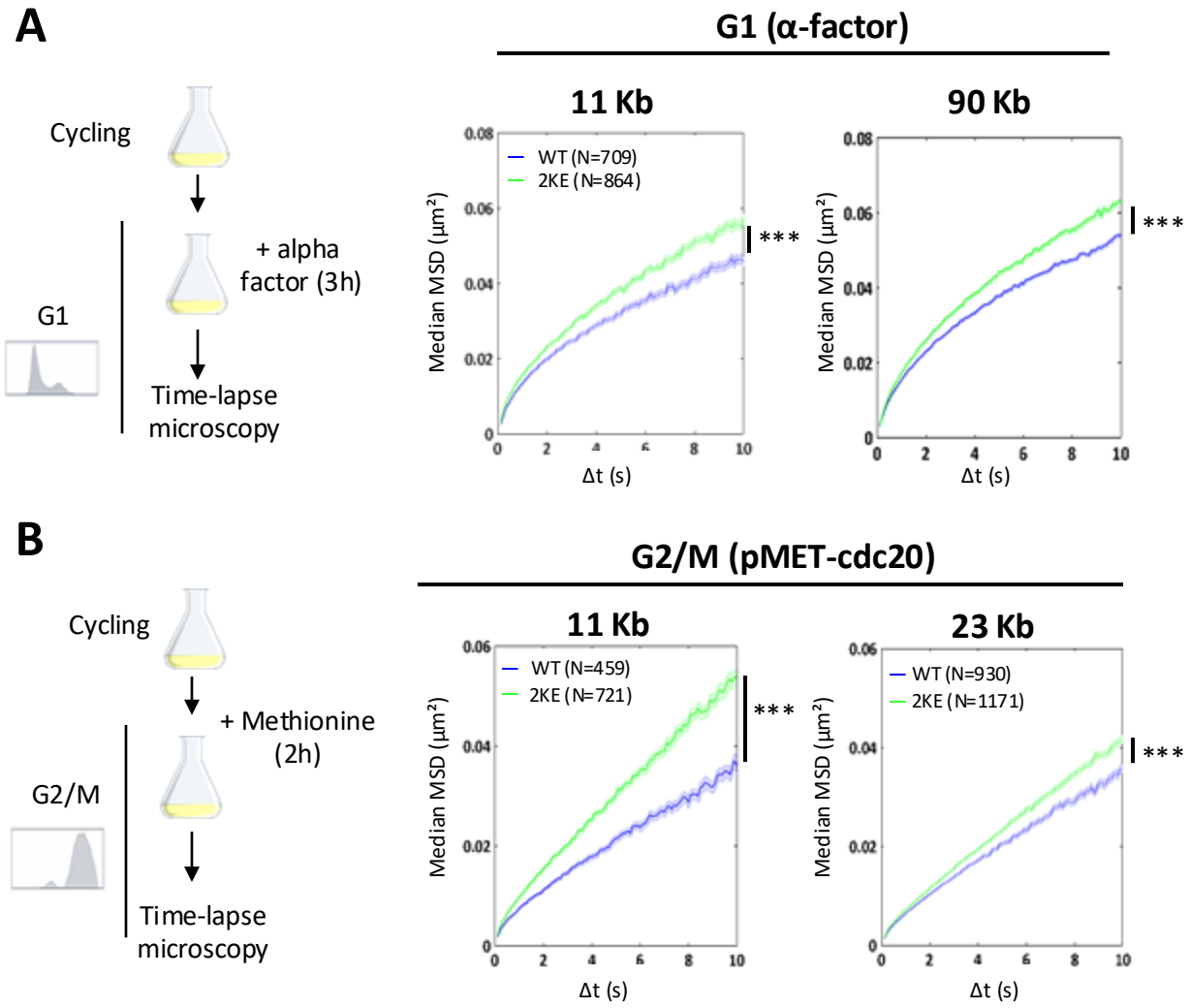

C

Cell phase	Tracked locus	Strain	MSD at 10 sec (10^{-2})	Alpha	D (10^{-3})	Cell number
G1	11 kb	WT	4.56	0.56	3.3	709
		smc5-2KE	5.72	0.56	3.8	864
	90 kb	WT	5.34	0.56	3.2	1838
		smc5-2KE	6.32	0.58	3.5	1623
G2/M	11 kb	WT	3.60	0.64	1.9	459
		smc5-2KE	5.38	0.67	2.5	865
	23 kb	WT	3.58	0.67	1.7	930
		smc5-2KE	4.18	0.69	1.8	1757

Figure supplement 5

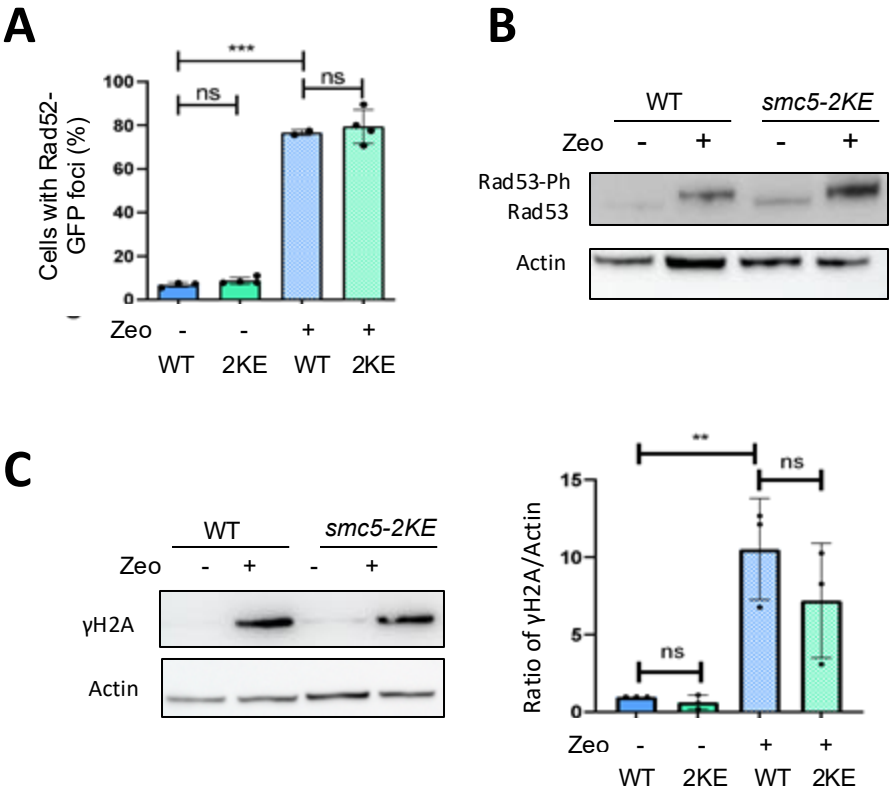

Figure supplement 6

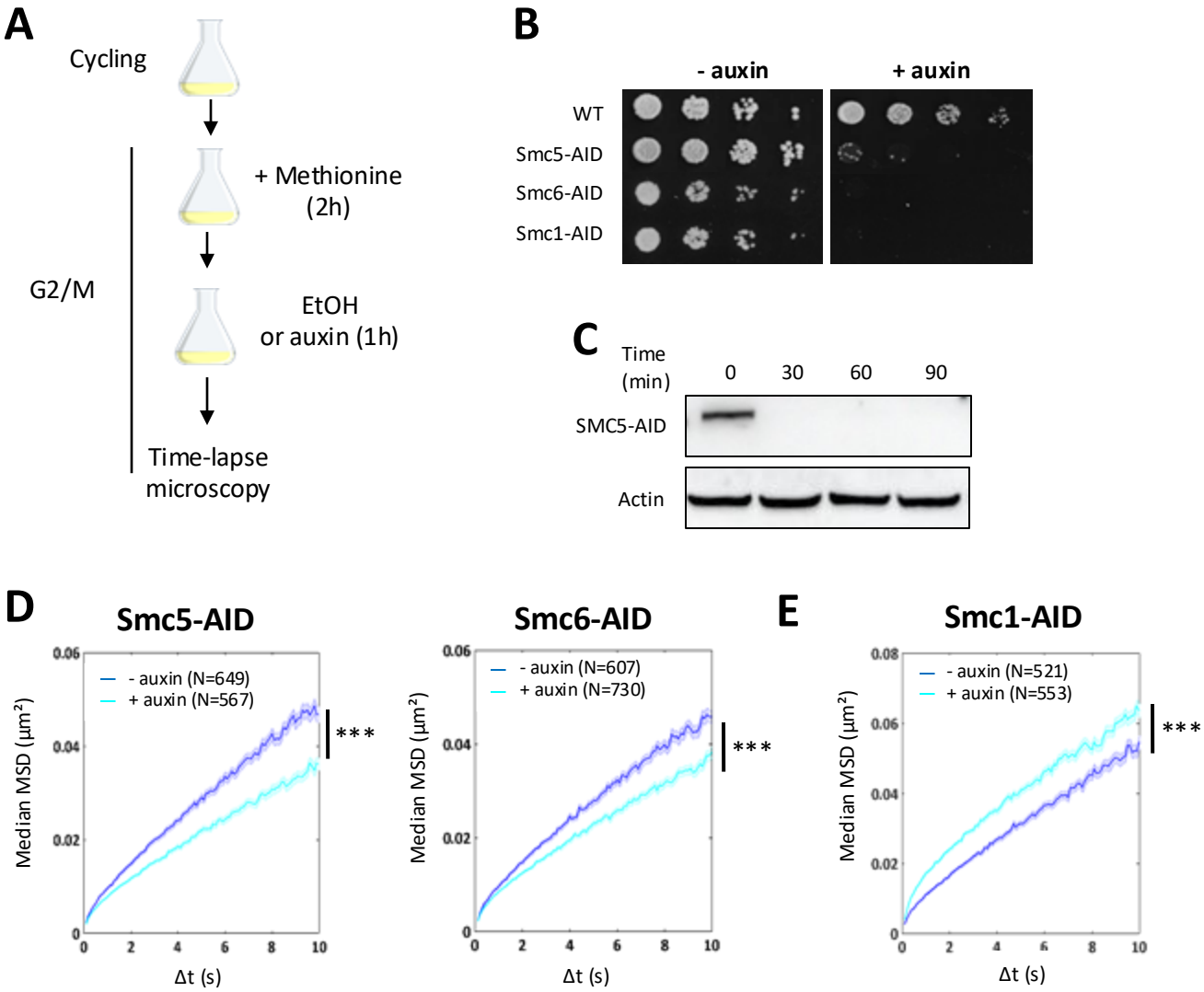

F

	Auxin	MSD at 10 sec (10^{-2})	Alpha	D (10^{-3})	Cell number
Smc5-AID	-	4.68	0.63	2.5	649
	+	3.62	0.61	1.9	567
Smc6-AID	-	4.59	0.64	2.5	607
	+	3.84	0.62	2.2	730
Smc1-AID	-	5.47	0.64	2.7	521
	+	6.34	0.58	4.1	553

Figure supplement 7

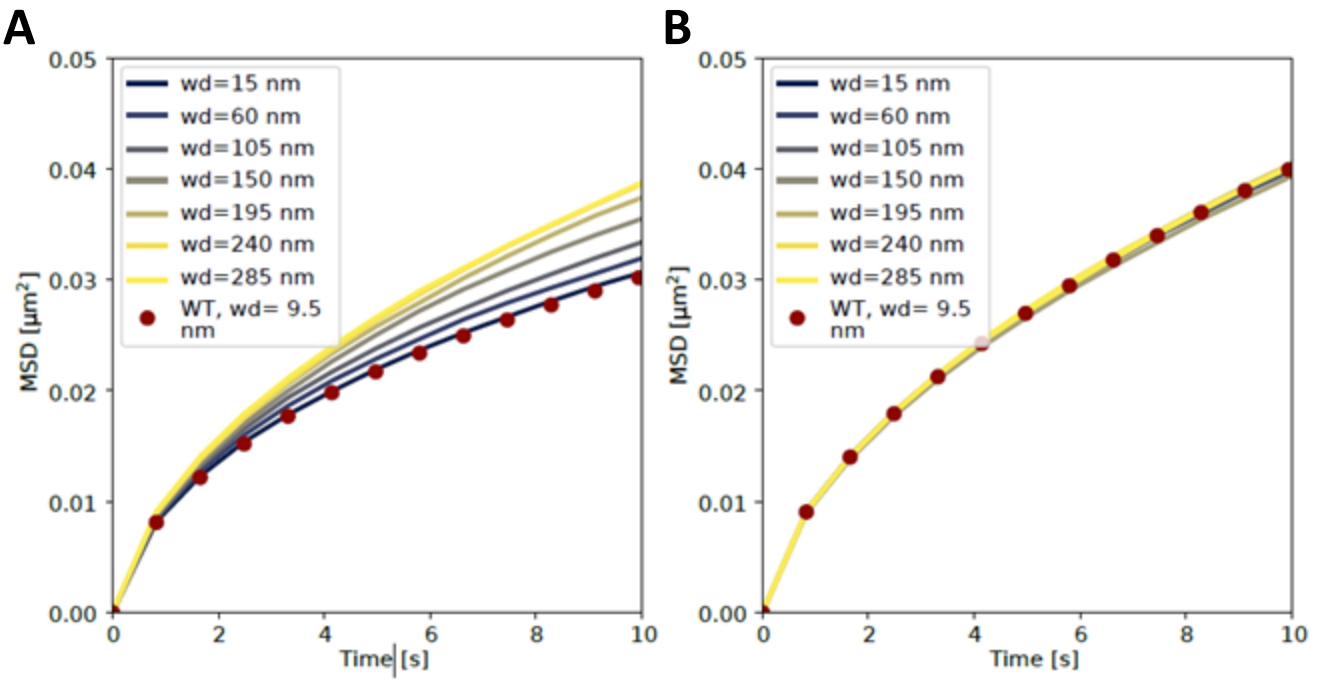

Figure supplement 8

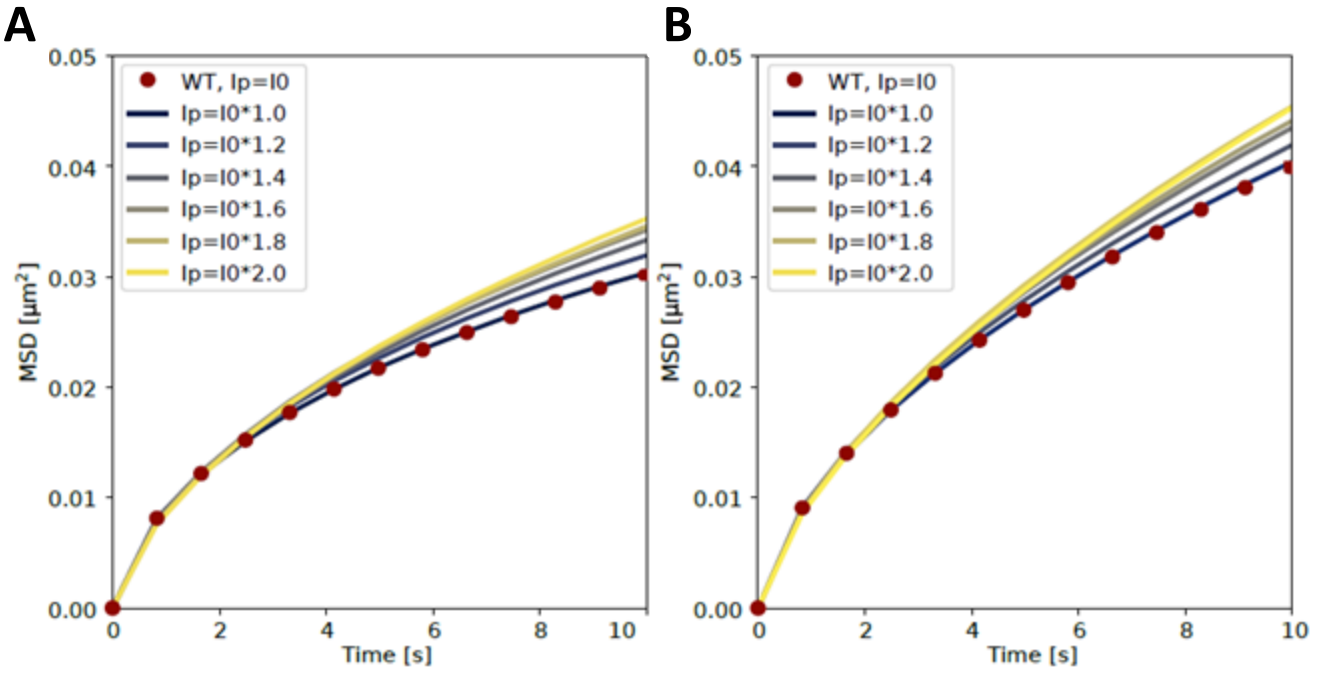

Figure supplement 9

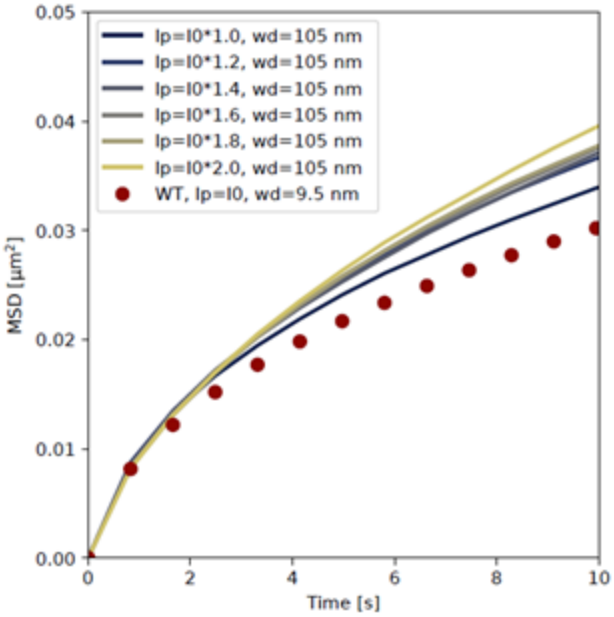

Figure supplement 10

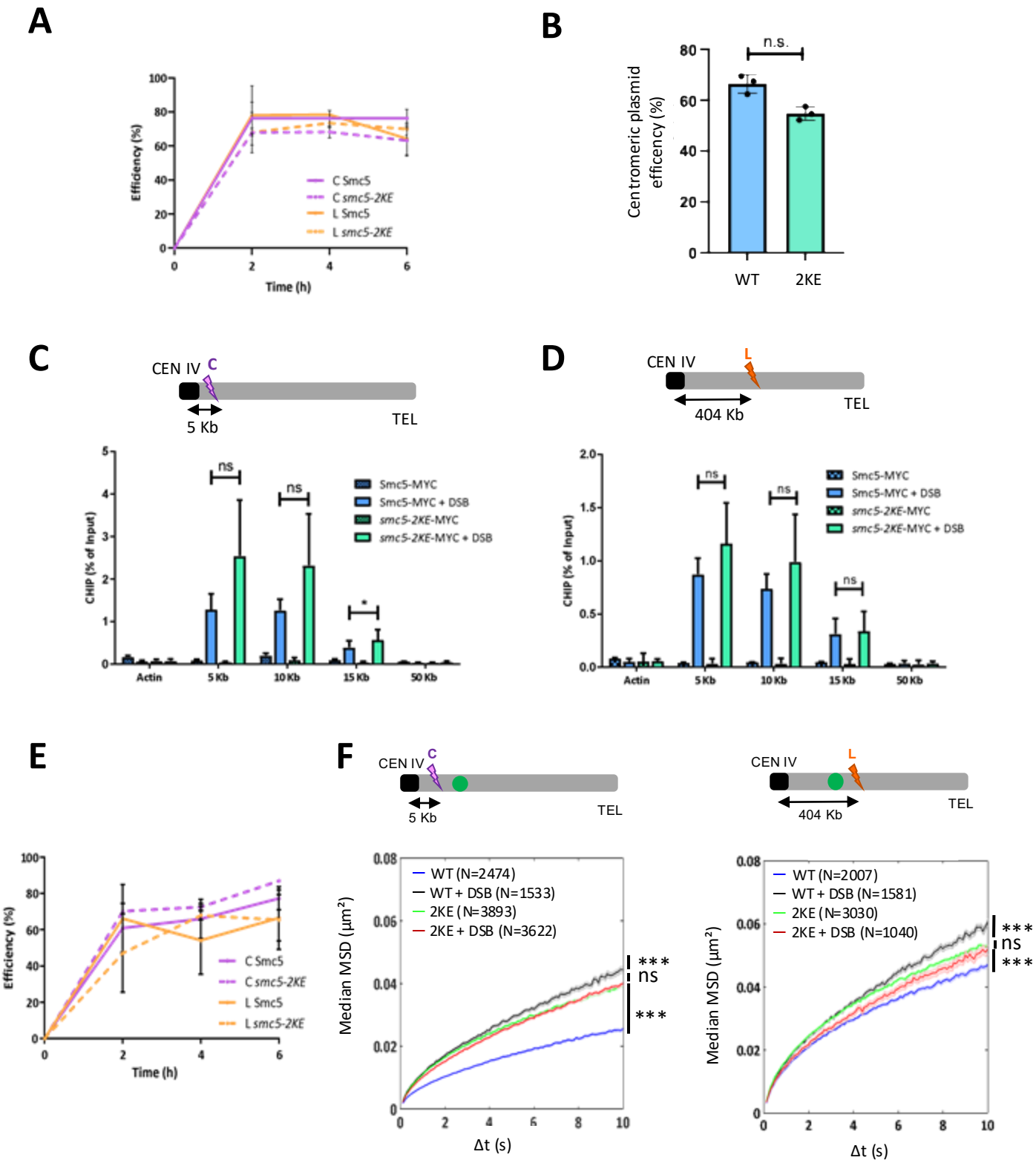

G

DSB position	Strain	DSB	MSD at 10 sec (10^{-2})	Alpha	D (10^{-3})	Cell number
C	WT	-	2.55	0.57	1.4	2474
		+	4.43	0.59	2.8	1533
	smc5-2KE	-	3.94	0.56	2.6	2893
		+	4.00	0.58	2.5	3622
L	WT	-	4.69	0.54	3.5	2007
		+	6.05	0.57	4.0	1581
	smc5-2KE	-	5.25	0.53	4.0	3030
		+	5.19	0.55	3.6	1040